Intracellular zinc is a critical intermediate in the excitotoxic cascade

Alberto Granzotto[a] and Stefano L. Sensi[a,b,c,d,1]

[a] Molecular Neurology Unit, Center of Excellence on Aging (Ce.S.I.), Chieti, Italy; [b] Department of Neuroscience and Imaging, University "G. d'Annunzio", Chieti, Italy; [c] Departments of Neurology and Pharmacology, University of California-Irvine, Irvine, CA, USA; [d] Institute for Memory Impairment and Neurological Disorders, University of California-Irvine, Irvine, CA, USA

[1] To whom correspondence should be addressed.

Stefano L. Sensi, MD, PhD

Ce.S.I. – Center of Excellence on Aging

Via Luigi Polacchi, 11

66100, Chieti (CH), Italy

Phone: +39 0871541544

Fax: +39 0871541542

E-mail: ssensi@uci.edu

Abstract

Excessive and sustained exposure to glutamate leads to injurious elevations of cytosolic calcium ($[Ca^{2+}]_i$), generation of reactive oxygen and nitrogen species (ROS, RNS), mitochondrial failure, mobilization of intracellular zinc ($[Zn^{2+}]_i$), and, ultimately, neuronal death. The relative contribution and temporal dynamics of the activation of these processes to promote the full development of excitotoxicity are still not completely understood. In this study, we exploited the unique features of nNOS positive neurons [nNOS (+)], a striatal subpopulation that is constitutively spared from NMDAR-dependent insults, and dissected NMDAR-driven $[Ca^{2+}]_i$, $[Zn^{2+}]_i$, ROS, and mitochondrial changes occurring in these neurons and the overall population of nNOS (-) striatal neurons. Comparing the two populations and employing pharmacological, biochemical, and single-cell imaging techniques, we show that $[Zn^{2+}]_i$ mobilization acts as critical intermediate in the cascade that links NMDAR-mediated ROS overproduction, mitochondrial failure, and $[Ca^{2+}]_i$ deregulation to the production of neuronal damage. Results of this study may also provide the rationale for aiming at therapeutic agents that favor Zn^{2+} homeostasis for the treatment of acute or chronic neurological conditions associated with excitotoxicity.

Keywords: calcium, glutamate, neuronal death, mitochondria, oxidative stress, nNOS

Introduction

Calcium (Ca^{2+}) entry through the activation of the ionotropic glutamate receptor N-methyl-D-aspartate (NMDAR) plays a pivotal role in the physiological modulation of neuronal functioning (Paoletti et al., 2013). However, upon acute or chronic neurological conditions like stroke, amyotrophic lateral sclerosis (ALS), Alzheimer's disease (AD), or Huntington's disease (HD), sustained NMDAR activation is crucial in promoting neuronal loss (Parsons and Raymond, 2014). The process has been described as excitotoxicity (Choi, 1988; Choi, 1992; Olney, 1969; Rothman and Olney, 1986) and, according to the excitotoxic cascade (Yu et al., 2001), massive Ca^{2+} entry through NMDARs sets in motion generation of reactive oxygen species (ROS) as well as PSD-95 dependent production of nitrogen species (RNS), mitochondrial failure, activation of Ca^{2+}-dependent proteases, and the initiation of apoptotic and necrotic signaling (Bano et al., 2005; Dugan et al., 1995; Sattler et al., 1999; Schinder et al., 1996). Ca^{2+} has been originally described as the major ionic determinant of excitotoxicity; however, evidence accumulated in the past two decades has indicated that zinc (Zn^{2+}), another divalent cation largely present in the brain, can also actively modulate the excitotoxic cascade (McCord and Aizenman, 2013; Sensi et al., 2009).

Like Ca^{2+}, Zn^{2+} can favor neuronal functioning but, when deregulated, the cation becomes a potent neurotoxic agent (Sensi et al., 2009). Upon excitotoxic stimuli, Zn^{2+} is released in a Ca^{2+}- and ROS/RNS-dependent manner from intracellular pools (Bossy-Wetzel et al., 2004; Sensi et al., 2003) and compelling evidence indicates that, once free in the cytosol, the cation targets mitochondria where, in close synergy with Ca^{2+}, promotes long lasting organelle dysfunctions that result in loss of the mitochondrial membrane potential ($\Delta\Psi$), excessive ROS production, opening of the mitochondrial permeability transition pore as well as the uncontrolled release of pro-apoptotic factors (Jiang et al., 2001; Sensi et al., 2000).

While it is clear that the two ions act in synergy, their relative contributions to the excitotoxic cascade have been only partially disclosed (Sensi et al., 2009; Shuttleworth and Weiss, 2011). To address this issue, we took advantage of the behavior and unique features of a small subpopulation of aspiny striatal interneurons

(<2% of the overall population in our cultures), the NADPH-diaphorase neurons, that overexpresses the neuronal isoform of the nitric oxide synthase enzyme (nNOS, also known as NOS1) (Dawson et al., 1991; Hope et al., 1991). These neurons have been shown to be spared from excitotoxic insults triggered by exposure to NMDAR agonists (i.e.: NMDA, quinolinate, aspartate; Koh and Choi, 1988; Koh et al., 1986). The investigation of this set of neurons bears clinical implications as the subpopulation [hereafter indicated as nNOS (+) neurons] is insensitive to excitotoxic insults triggered in the striatum (Beal et al., 1993) and found largely spared in striata of HD patients (Ferrante et al., 1985). HD is a genetic disorder characterized by the aberrant expansion of the trinucleotide CAG repeat within the gene encoding for the huntingtin protein resulting in the production of neurotoxic polyQ-Htt (The Huntington's Disease Collaborative Research Group, 1993). PolyQ-Htt, in addition to other mechanisms like impaired vesicle trafficking, perturbation of synaptic activity, disruption of neurotrophic signaling, defective mitochondrial functioning and morphology, is also known to promote neuronal death throughout the modulation of NMDAR activity. The phenomenon is particularly prominent in the striatum, a highly HD-vulnerable region, where polyQ-Htt leads to the increased susceptibility to excitotoxic insults (Cowan and Raymond, 2006; Ross and Tabrizi, 2011).

Deciphering the molecular determinants of nNOS (+) resistance to excitotoxicity has also important value in the context of neurological conditions associated with glutamate-driven injury. This is the case for neurodegenerative settings like AD, where β-amyloid peptides have been shown to impair Ca^{2+} homeostasis and increase susceptibility to glutamate-dependent neurotoxicity (Mattson et al., 1992), or ALS, where excitotoxicity plays a pivotal role in the early stages of motor neuron (MN) demise (Boillee et al., 2006; Rothstein et al., 1995). Sustained NMDAR activation and associated excitotoxicity is also a major component of the neuronal loss found in cerebral ischemia (Aarts et al., 2002; Choi, 1996; Rothman and Olney, 1986).

Interestingly, nNOS (+) neurons show insensitivity to NMDAR-mediated toxicity even though the cells express abundant mRNA levels for different NMDAR subunits (Landwehrmeyer et al., 1995; Price et al., 1993) and respond to NMDA exposures with $[Ca^{2+}]_i$ rises (an indirect index of receptor functioning) that are largely overlapping with those occurring in neighboring nNOS (-) neurons (Canzoniero et al., 2013). Indicating that most

of the resistance to NMDAR activation is due to modifications of downstream mechanisms, the subpopulation has been shown to fail to generate ROS of mitochondrial origin in response to sustained receptor activation (Canzoniero et al., 2013). This decreased NMDAR-driven oxidative stress is likely related to the fact that nNOS (+) neurons are potentially exposed to an intracellular environment that is chronically enriched with large amounts of nitric oxide (NO), the oxidative species that is known to be a major determinant of NMDAR-mediated toxicity (Lau and Tymianski, 2010; Sattler et al., 1999). Thus, it is conceivable that, to prevent injurious effects of peroxynitrite, nNOS (+) neurons are driven to constitutively express high levels of ROS scavenging enzymes (Bidmon et al., 2001; Gonzalez-Zulueta et al., 1998), thereby making the subpopulation better equipped to deal with the oxidative hit produced by NMDAR overactivation (Canzoniero et al., 2013). In that respect, nNOS (+) have shown to express high levels of SOD2, the enzyme in charge of the quenching of mitochondrial ROS (Gonzalez-Zulueta et al., 1998). Therefore, nNOS (+) neurons represent an ideal physiological setting to investigate how oxidative stress acts in the production of downstream events linked to the excitotoxic cascade. In that regard, it should be underlined that oxidative stress is closely associated with the deregulation of intraneuronal Zn^{2+} ($[Zn^{2+}]_i$) as Ca^{2+}-dependent generation of ROS and NMDAR-mediated RNS production lead to neurotoxic $[Zn^{2+}]_i$ release from intracellular sites like the metallothioneins (MTs), a major cytosolic system for Zn^{2+} buffering that is redox sensitive and prone to release the cation upon oxidation (Aizenman et al., 2000; Bossy-Wetzel et al., 2004; Maret, 1994). Thus, nNOS (+) neurons also offer a perfect experimental setting that can help to dissect the interplay between Ca^{2+} and Zn^{2+} in the production of excitotoxic injury.

To gain insight on these mechanisms, in this study, we combined pharmacological, biochemical, and single-cell imaging techniques and analyzed NMDAR-driven changes in $[Ca^{2+}]_i$ and $[Zn^{2+}]_i$ levels as well as modifications of mitochondrial functions (a point of convergence in the excitotoxic cascade) in cultured striatal nNOS (+) and nNOS (-) neurons. Alterations occurring in the two populations were compared to reveal differences in downstream mechanisms of excitotoxicity.

Materials and methods

Materials

All cell culture media and sera were bought from GIBCO (Life Technologies). All fluorescent indicators (FluoZin-3 AM, fluo-4 AM, fluo-4FF AM, Mag-fura-2 AM and TMRE) were purchased from Molecular Probes (Life Technologies). All the other chemicals were purchased from Sigma-Aldrich (unless otherwise specified).

Neuronal striatal cultures

All the procedures involving animals were approved by the institutional Ethics Committee (CEISA prot. PROG21) and performed in accordance with institutional guidelines and national and international laws and policies. Female mice were caged in groups of 3-4 animals while male mice were single-housed. Mice had *ad libitum* access to food and water and kept on a 12:12 light/dark cycle. All efforts were made to minimize animal suffering.

Neuronal striatal cultures were prepared from fetal CD1 mice at 15 or 16 days of gestation, as previously described (Canzoniero et al., 2013). Briefly, striatal tissues were dissected in an ice-cold dissecting medium, minced with forceps, and transferred in a 0.25% trypsin solution for 10 min at 37° C. Striata were then centrifuged at 1300 rpm, 4° C for 5 min, supernatant discarded and pellet dissociated with a fire-polished glass pipette. Dissociated cells were then re-suspended in Neurobasal medium supplemented with 0.5 mM L-Glutammine, 5% fetal bovine serum, 5% horse serum, 1x B27 and 0.2% penicillin/streptomycin and plated onto pre-treated laminin/poly-DL-lysine coated tissue culture plates or dishes. In order to obtain near-pure striatal cultures, three days after plating, non-neuronal cell growth was inhibited by adding 5 µM of cytosine arabinofuranoside. Every three days 25% of the medium was replaced with fresh Neurobasal. Experiments were performed on cultures between 12 and 18 days in vitro (DIV).

Cell viability assay

Neuronal death produced by an excitotoxic challenge (50 µM NMDA + 10 µM glycine) was evaluated by employing, with slight modifications, lactate dehydrogenase (LDH) efflux or propidium iodide (PI) staining protocols (Koh and Choi, 1987; Sattler et al., 1997).

For LDH assay, 12 h after excitotoxic challenge and/or pharmacological manipulation, 50 µl of bathing medium were collected in a 96-well plate and diluted with 225 µl of intracellular phosphate buffered solution containing pyruvate (0.23 mg/ml) and NADH (Merck-Millipore; 0.11 mg/ml). LDH-dependent conversion of NADH to NAD^+ was monitored at 340 nm in a Spectramax 190 plate reader (Molecular Devices). A small amount of LDH is present in the media of cultures sham washed; this release (blank) was assessed in sister cultures for each experiment and subtracted from all values to yield signals specifically associated with NMDA exposures. Each experiment also included a set of sister cultures exposed to 300 µM NMDA for 24 h, a maneuver that induces virtually complete neuronal loss without glial death (full kill). To determine the percentage of neuronal death, LDH efflux from treatment conditions was divided by LDH efflux in full kill samples.

PI staining was performed to detect damaged nuclei, an indirect index of cell death. 24 h after excitotoxic stimulation cells were rinsed three times in HCSS and incubated for 1 h at room temperature with a PI loading solution (in mM: 121 NaCl, 5 KCl, 20 glucose, 10 Hepes, 7 Hepes-Na, 3 $NaHCO_3$, 1 sodium pyruvate, 1.8 $CaCl_2$, 0.01 glycine, and 0.01 mg/ml of propidium iodide). Cells were then washed with TBS, fixed for 30 min at 4° C in 4% paraformaldehyde/0.1 M PBS buffer and stained for nNOS (+) neurons (see below). For each dish, six differential interference contrast (DIC) images were randomly acquired and, using ImageJ (Schindelin et al., 2012), merged with those obtained with PI fluorescence staining (Ex λ: 530 nm, Em λ: 575-610). PI-positive nuclei were manually counted using the cell counter ImageJ plugin tool and normalized to the number of cells present in each DIC field. After subtraction of fluorescence background, only cells showing a clear nuclear staining were considered to be PI-positive. The percentage of live neurons in control dishes was set at 100% and the % of cell death in treated dishes was normalized accordingly. The percentage of intact nNOS (+) neurons identified after treatments was normalized to the average number of nNOS (+) neurons present in untreated cultures.

Live-cell imaging

Live-cell imaging experiments were performed by employing an Axio Examiner.D1 upright microscope (Zeiss) equipped with a Xenon lamp-based Optoscan monochromator (Cairn), a 20x W Plan-Apochromat (N.A.: 1.0; Zeiss) objective and a 16-bit Evolve 512 EMCCD camera (Photometrics). Image acquisition and storage for offline analysis was performed by using Metamorph 7.7 software (Molecular Devices).

$[Ca^{2+}]_i$ and $[Zn^{2+}]_i$ measurements

Striatal cultures were loaded in the dark for 30 min with fluo-4 AM (3 µM), fluo-4FF AM (3 µM), FluoZin-3 AM (4 µM), or Mag-fura-2 (5 µM) plus 0.1% Pluronic F-127 in a HEPES-buffered saline solution (HCSS) whose composition was (in mM): 120 NaCl, 5.4 KCl, 0.8 $MgCl_2$, 20 HEPES, 15 glucose, 1.8 $CaCl_2$, 10 NaOH, pH 7.4, washed, and incubated in the dark for further 30 min in HCSS. No macroscopic differences in cytosolic distribution of dye loading were observed in the two populations. Fluo-4 AM, fluo-4FF AM or FluoZin-3 AM (Ex λ: 478 ± 15 nm, Em λ: 525 nm) fluorescence changes of each cell were expressed as ΔF/F, where F is the basal fluorescence intensity and ΔF the relative fluorescence change (F_x-F). Mag-fura-2 AM (Ex λ: 340 ± 10 nm, 380 ± 10 nm, Em λ: 510 nm) fluorescence changes of each cell were expressed as 340/380 emission ratio. In Mag-fura-2 AM experiments, 1 µM TPEN was added to the medium to avoid $[Zn^{2+}]_i$ interferences with $[Ca^{2+}]_i$-dependent fluorescence signals (Hyrc et al., 2000). In experiments carried out in HCSS without Na^+ and Ca^{2+} NaCl was replaced with N-methyl-D-glucamine (130 mM) and $CaCl_2$ was omitted from the final solution. High K^+ HCSS was obtained by replacing 60 mM NaCl with 60 mM KCl. Pharmacological stimulations were applied at the indicated time points and washed out employing a perfusion system running at an average rate of 0.5 ml/min (Biologic). All loading procedures and recordings were carried out at room temperature.

ROS measurements

Detection of reactive oxygen species (ROS) production was monitored by employing dihydroethidium (HEt; Ex λ: 510 ± 15 nm, Em λ: 575-610 nm), an oxidation-sensitive dye. Striatal neurons were loaded in the dark

for 45 min with 5 μM HEt in HCSS. After baseline fluorescence acquisition, NMDAR stimulation was performed by adding NMDA (50 μM) + glycine (10 μM) for 5 min and then halted by adding the selective non-competitive NMDAR blocker MK-801 (10 μM) to the bathing solution. HEt was kept in the buffer throughout all the imaging sessions in order to maintain dye equilibration. HEt data are reported as ΔF/F.

Measurements of mitochondrial ΔΨ

Measurements of the mitochondrial membrane potential (ΔΨ) were performed by loading striatal neurons with 50 nM of the tetramethyl rhodamine ethyl ester (TMRE) for 30 min in HCSS at room temperature. TMRE fluorescence (Ex λ: 510 ± 15 nm, Em λ: 575-610 nm) changes of each cell (F_x) were normalized to basal fluorescence intensity (F_0).

NADPH-diaphorase staining

nNOS (+) neurons were detected, as previously described (Canzoniero et al., 2013), by employing the NADPH-diaphorase staining procedure. Briefly, after Ca^{2+}, Zn^{2+}, HEt, TMRE or PI experiments, cultures were rinsed three times in ice-cold TBS and fixed for 30 min at 4° C in 4% paraformaldehyde/0.1 M PBS buffer. After fixation, dishes were washed with large volumes of TBS, permeabilized for 5 min with 0.2% Triton X-100/TBS and stained for 1h at 37° C in a humidified chamber with NADPH-diaphorase staining solution. NADPH-diaphorase staining solution contained: 0.1 M Tris/HCl, 0.2% Triton X-100, 1.2 mM sodium azide, 0.2 mM nitrotetrazolium blue, and 1 mM NADPH (Merck), pH 7.2. The staining solution was then removed and cultures rinsed with TBS. Dishes were re-inserted in the microscope stage and, using DIC, fields were re-matched with those previously imaged with fluo-4 AM, fluo-4FF AM, fluoZin-3 AM, Mag-fura-2, HEt, or TMRE. Identified nNOS (+) neurons were then evaluated for their responses in fluorescence imaging experiments and compared with those of neighboring nNOS (-) neurons.

Data representation and statistical analysis

Normalized fluorescence values of intracellular dynamics are analyzed in terms of peak amplitude (as index of maximum cation load, maximum $\Delta\Psi$ loss or ROS generation and area under the curve (a.u.; an index of overall cation or ROS load).

Data are represented as box plots. Center lines show medians, center boxes represent means, box limits indicate 25th and 75th percentiles, whiskers extend 1.5 times the interquartile range from the 25th and 75th percentiles. Outliers are represented by open circles (Krzywinski and Altman, 2014).

LDH efflux assay ad high K^+ experiments are reported as mean ± SEM.

Bartlett's test was performed to assess homogeneity of variances. If variances significantly differed, statistical comparison of normalized data was performed using Welch's corrected unpaired t-test, otherwise Student's t-test was employed. High K^+ viability assay was analyzed by ANOVA followed by Dunnett's post-hoc test. P values are represented as * for $P \leq 0.05$ and ** for $P \leq 0.01$.

Results

nNOS (+) neurons are spared from excitotoxic insults and show improved $[Ca^{2+}]_i$ handling after NMDA exposure

In the first set of experiments, we investigated the viability of nNOS (+) and nNOS (-) striatal neurons upon an acute excitotoxic challenge (50 μM NMDA + 10 μM glycine for 5 min). Viability was assayed by staining neurons with the apoptotic marker propidium iodide (PI) or by assessing the average number of surviving nNOS (+) neurons in NMDA-treated dishes or in sham-washed sister cultures. As expected, NMDA promoted, within 24 h, a major loss of nNOS (-) neurons (53.4±4.7% death; Fig. 1A and B) while nNOS (+) neurons were largely spared as shown by the retention of nNOS enzymatic activity and the preserved neuronal morphology (Fig. 1A and B; Ferrante et al., 1985; Koh et al., 1986; Uemura et al., 1990).

Using Ca^{2+} imaging, we have previously shown that nNOS (+) neurons possess functional NMDARs and are able to promote rapid $[Ca^{2+}]_i$ rises that are indistinguishable from the ones found in neighboring nNOS (-) neurons (Canzoniero et al., 2013). Confirming these previous findings, brief exposure (20 seconds) to NMDA (50 µM) + glycine (10 µM) produced overlapping cytosolic $[Ca^{2+}]_i$ rises in nNOS (+) and nNOS (-) striatal neurons (Fig. S1). In order to further dissect NMDAR-driven $[Ca^{2+}]_i$ changes in the two neuronal populations, striatal cultures were loaded with the low affinity Ca^{2+} indicator fluo-4FF (K_d=9.7 µM), and $[Ca^{2+}]_i$ elevations monitored during and after a 5 min NMDA (50 µM) + glycine (10 µM) exposure. Compared to nNOS (-) cells, nNOS (+) neurons showed reduction of $[Ca^{2+}]_i$ rises that are occurring 90 sec after NMDAR activation (Fig 1C and D). nNOS (+) neurons also showed improved $[Ca^{2+}]_i$ clearance during the washout phase [Fig. 1E; peak fluo-4FF levels in nNOS (-): 8.42±0.21 *vs* 4.09±0.35 in nNOS (+); area under the curve (AUC): 1029.7±57.9 in nNOS (-) *vs* 423.7±75.6 in nNOS (+)]. In a second set of experiments, we tested whether nNOS (+) neurons show differences as far as routes of Ca^{2+} entry, like the voltage-gated calcium channels (VGCCs), that are synergistically activated by NMDA. To that aim, VGCC behavior was studied in fluo-4FF-loaded striatal neurons exposed to a depolarizing medium [high K^+ (60 mM K^+)] in presence of full glutamatergic inhibition [MK-801, 10 µM (to block NMDARs) and 2,3-dihydroxy-6-nitro-7-sulfamoylbenzo[f]quinoxaline (NBQX), 10 µM (to block AMPARs)]. Experiments were performed with a high acquisition rate (50 frames per second) and the resulting fast Ca^{2+} imaging traces revealed that nNOS (+) neurons did not differ in terms of VGCC responses when compared to nNOS (-) neurons [Fig. 1F-H and S2; peak fluo-4FF levels in nNOS (-): 4.84±0.06 *vs* 5.00±0.41 in nNOS (+); AUC: 782.9±11.8 in nNOS (-) *vs* 768.8±61.6 in nNOS (+)].

Findings of this set of experiments suggest that, in nNOS (+) neurons, decreased NMDAR-driven $[Ca^{2+}]_i$ levels are not depending on reduced Ca^{2+} entry but rather resulting from the activation of more efficient Ca^{2+} buffering systems.

nNOS (+) neurons retain mitochondrial ΔΨ upon NMDA exposure

Mitochondria play a key role in the excitotoxic cascade (Nicholls, 2009; Schinder et al., 1996) and we therefore evaluated possible differences, between the two striatal neuronal populations, as far as mitochondrial responses to NMDA exposure. To that aim, we investigated NMDAR-driven changes of the mitochondrial membrane potential (ΔΨ) in nNOS (-) and nNOS (+) neurons loaded with tetramethylrhodamine ethyl ester (TMRE), a ΔΨ-sensitive dye. After baseline acquisition, striatal neurons were challenged with NMDA (50 µM) + glycine (10 µM) and TMRE fluorescence changes evaluated for up to 30 min. In this set of experiments, nNOS (-) neurons responded to NMDA with a prompt decrease in TMRE fluorescence, a phenomenon indicative of acute ΔΨ loss (Fig. 2A-D; peak TMRE fluorescence changes: 0.49±0.008). On the contrary, in nNOS (+) neurons, NMDAR stimulation induced only a modest ΔΨ loss (Fig. 2A-D; peak TMRE fluorescence changes: 0.80±0.04), thereby indicating that the subpopulation may contain mitochondria that are less sensitive to the deregulatory effects of NMDAR activation. The phenomenon is likely to be specific on the route of Ca^{2+} entry and modulated by factors that work in addition to $[Ca^{2+}]_i$ rises. This is in agreement with the idea that selective coupling of NMDAR activation to NO production, via PSD-95 activation, initiates a set of unique downstream pathways that promotes damaging accumulation of ROS and RNS (Dugan et al., 1995; Sattler et al., 1999). Supporting this assumption, control experiments in which nNOS (-) and nNOS (+) neurons were exposed to a depolarizing medium (60 mM K^+ with MK-801 10 µM and NBQX 10 µM) in order to activate VCGCCs, revealed that the two neuronal populations exhibit overlapping $[Ca^{2+}]_i$ rises (Fig. 1F-H and S3A-C), negligible ROS production and $[Zn^{2+}]_i$ rises as well as modest ΔΨ changes (Fig. S3).

nNOS (+) neurons exposed to NMDA show improved mitochondria-mediated $[Ca^{2+}]_i$ buffering

Mitochondria represent a major buffering system that helps cells to cope with $[Ca^{2+}]_i$ accumulations (Giacomello et al., 2007; Rizzuto et al., 2012). The mitochondrial Ca^{2+} buffering activity was therefore tested and compared in the two striatal populations. To that aim, striatal cultures were loaded with the low affinity Ca^{2+} indicator Mag-fura-2 (K_d=20 µM; Hyrc et al., 2000). We chose Mag-fura-2 as the probe exhibits a Ca^{2+} affinity

that is lower than fluo4-FF and therefore more suitable to detect the expected large $[Ca^{2+}]_i$ rises triggered by NMDAR activation. Mag-fura-2 loaded neurons were exposed to NMDA (50 µM) + glycine (10 µM) in presence of carbonyl cyanide 3-chlorophenylhydrazone (CCCP; 750 nM), a mitochondrial uncoupler that depolarizes the organelles, thereby abolishing the driving force needed for mitochondrial Ca^{2+} uptake. After CCCP exposures, NMDAR-driven $[Ca^{2+}]_i$ rises occurring in nNOS (+) neurons were found to be largely similar to those observed in nNOS (-) cells [Fig. 2 E-G; peak levels: 0.82±0.007 in nNOS (-) *vs* 0.76±0.03 in nNOS (+); AUC: 41.5±0.65 in nNOS (-) *vs* 32.0±2.35 in nNOS (-)]. These results indicate that, when the mitochondrial Ca^{2+} buffering capacity is ruled out, Ca^{2+} influx though NMDARs produces similar levels of cation overload in the two subpopulations.

To further dissect the role of mitochondria in nNOS (+) neurons, we investigated dynamics of mitochondrial Ca^{2+} changes that occurred in the recovery phase that followed brief NMDA exposure and agonist washout. To that aim, striatal neurons, loaded with fluo-4 (K_d=335 nM), were exposed for 90 sec to NMDA (50 µM) + glycine (10 µM) in presence of cyclopiazonic acid (CPA 10 µM), a sarco/endoplasmic reticulum (ER) Ca^{2+}-ATPase inhibitor. Use of CPA, by blocking the ER component, allows the investigation of mitochondrial Ca^{2+} uptake. After recovery to baseline $[Ca^{2+}]_i$ values, cultures were stimulated with CCCP (5µM), here used at a higher concentration to promote full cytosolic unloading of mitochondrial Ca^{2+}. CCCP exposures were carried out in nominally Ca^{2+}- and Na^{+}-free solutions to prevent ion influx from the extracellular space and isolate intracellular-related changes. Results of the experiments show that mitochondrial Ca^{2+} release is significantly higher in nNOS (-) neurons when compared to nNOS (+) cells, [Fig. 2H-J; peak fluo-4 levels: 2.43±0.07 in nNOS (-) *vs* 1.5±0.24 in nNOS (+); AUC: 176.5±5.12 in nNOS (-) *vs* 111.5±17.2 in nNOS (+)], thereby suggesting improved Ca^{2+} cycling in the organelles of nNOS (+) neurons.

nNOS (+) neurons show reduced ROS generation upon NMDA exposures

We have previously shown that nNOS (+) neurons fail to generate mitochondrial ROS in response to an excitotoxic challenge (Canzoniero et al., 2013). However, it should be underlined that, upon NMDAR activation, other cytosolic sources (i.e.: the activation of NADPH oxidase) are available and can contribute to ROS

production (Brennan et al., 2009). We therefore evaluated the role of ROS of cytosolic origin. To that aim, striatal cultures, loaded with the ROS-sensitive dye dihydroethidium (HEt) were exposed to NMDA (50 μM) + glycine (10 μM) for 5 min and HEt fluorescence changes evaluated for up to 30 min. In line with other reports, nNOS (-) neurons showed rapid increases in HEt fluorescence following NMDA exposures (peak HEt levels: 2.15±0.05; AUC: 18.6±0.42) while nNOS (+) neurons exhibited largely decreased NMDA-driven HEt fluorescence changes (Fig. 3A-E; peak: 0.68±0.08; AUC: 6.6±0.68). These findings, along with the known overexpression, in nNOS (+) neurons, of SOD2 (Gonzalez-Zulueta et al., 1998), support the idea that this neuronal subpopulation may be particularly efficient in quenching ROS of mitochondrial origin.

nNOS (+) neurons show largely decreased mobilization of $[Zn^{2+}]_i$ upon NMDA exposure

As intracellular release of Zn^{2+} is dependent on $[Ca^{2+}]_i$ rises and the ROS/RNS production set in motion by overactivated ionotropic glutamatergic receptors (Aizenman et al., 2000; Bossy-Wetzel et al., 2004; Sensi et al., 2003), we then investigated and compared NMDAR-driven $[Zn^{2+}]_i$ rises occurring in the two neuronal populations. To that aim, striatal cultures were loaded with the Zn^{2+}-sensitive [and Ca^{2+}-insensitive (Zhao et al., 2008)] probe FluoZin-3 (K_d=15 nM; Gee et al., 2002). After baseline acquisition, FluoZin-3-loaded cultures were evaluated during and after a 5 min exposure to NMDA (50 μM) + glycine (10 μM). In agreement with previous studies, NMDAR activation was found to induce rapid and reversible $[Zn^{2+}]_i$ rises in nNOS (-) neurons [Fig. 4A-D, peak: 2.76±0.04; AUC: 262.6±6.2]. $[Zn^{2+}]_i$ elevations were instead found significantly reduced in nNOS (+) neurons (Fig. 4A-D; peak: 0.77±0.11; AUC: 65.6±17.4). To address whether this reduced $[Zn^{2+}]_i$ mobilization that occurs in nNOS (+) neurons is due to decreased availability and/or reduced presence of $Zn^{2+}{}_i$ pools, FluoZin-3-loaded cultures were stimulated with the disulfide oxidizing compound 2,2'-dithiodipyridine [DTDP, 250 μM, a molecule that has been successfully employed to mobilize $Zn^{2+}{}_i$ (Aizenman et al., 2000)]. Largely overlapping DTDP-dependent $[Zn^{2+}]_i$ elevations were found in the two striatal subpopulations [Fig. 4E-H; peak: 10.04±0.09 in nNOS (-) *vs* 9.4±0.65 in nNOS (+); AUC: 1245.9±10.8 in nNOS (-) *vs* 1117.6±62.6 in nNOS (+)], thereby indicating that, in nNOS (+) and nNOS (-) neurons, availability of $Zn^{2+}{}_i$ is the same.

Finally, we tested whether nNOS (+) neurons show less susceptibility to Zn^{2+}-dependent toxicity. To that aim, we evaluated the viability of striatal cultures exposed to exogenous Zn^{2+}. Exposure to extracellular Zn^{2+} (100 µM, for 20 min) in presence of a depolarizing medium [60 mM K^+ + MK-801 10 µM and NBQX 10 µM] to allow cation entry through VGCCs (Sensi et al., 1997), promoted, 24 h later, significant levels of neuronal death in the two populations (Fig. 4I-J). These results indicate that nNOS (+) neurons are not insensitive to Zn^{2+}-dependent neuronal injury.

Zn^{2+} chelation improves $[Ca^{2+}]_i$ handling, reduces mitochondrial ΔΨ loss, and attenuates NMDA-induced neuronal death in nNOS (-) neurons

In light of all the previous findings indicating a strong role for $[Zn^{2+}]_i$ elevations in the excitotoxic cascade, we evaluated whether pharmacological blockade of releasable Zn^{2+} in nNOS (-) neurons can reproduce the aborted excitotoxic cascade found in nNOS (+) cells and favor some levels of neuroprotection against NMDA-induced toxicity (Fig. 1C-E and 2A-D). At first, we investigated effects of Zn^{2+} chelation on NMDAR-driven $[Ca^{2+}]_i$ rises. To that aim, large (µM range) $[Ca^{2+}]_i$ changes were studied in striatal nNOS (-) neurons loaded with fluo-4FF and exposed to NMDA (50 µM) + glycine (10 µM) with or without the addition of N,N,N',N'-tetrakis(2-pyridylmethyl)ethylenediamine (TPEN; 10 µM), a high affinity cell-permeable Zn^{2+} chelator (K_d=0.7 fM; Radford and Lippard, 2013). TPEN was present in the experimental solutions before, during, and after NMDAR stimulation. Results of the experiments indicate that Zn^{2+} chelation did not affect the rapid phase of Ca^{2+} entry (Fig. 5A and B; peak: 10.26±0.27 in control *vs* 9.99±0.26 in TPEN-treated cultures) but improved $[Ca^{2+}]_i$ clearance upon agonist washout (Fig. 5C; AUC: 2130±79.1 in control *vs* 1407.8±61.1 in TPEN-treated cultures). Intriguingly, the phenomenon reproduced handling of NMDAR- mediated $[Ca^{2+}]_i$ rises observed in nNOS (+) neurons (Fig. 1C and E).

As discussed above, Zn^{2+} is a potent trigger of glutamatergic mitochondrial dysfunction (Bonanni et al., 2006; Sensi et al., 2003). Thus, to evaluate the contribution of $[Zn^{2+}]_i$ rises in NMDAR-dependent mitochondrial dysfunction, TMRE-loaded neurons were challenged with NMDA (50 µM) + glycine (10 µM) in presence of TPEN

(10 μM). In this set of experiments, Zn^{2+} chelation was found to significantly reduce NMDA-driven ΔΨ loss (Fig. 5D-E; peak: 0.61±0.009 in control *vs* 0.73±0.01 TPEN-treated cultures). In addition, the temporal profile of TPEN-mediated ΔΨ changes appears to be closely linked, and functionally interrelated, with the undergoing dynamics of $[Ca^{2+}]_i$ accumulation (Fig. 6C-D). In that respect, TPEN-mediated reduction of NMDA-dependent ΔΨ loss is paralleled by improved clearance of post-NMDA $[Ca^{2+}]_i$ loads, while, in untreated cultures, more profound ΔΨ losses are paired by sustained post-NMDA $[Ca^{2+}]_i$ accumulation and decreased rate of recovery of $[Ca^{2+}]_i$ to baseline values. These findings corroborate the hypothesis that inhibition of the negative effects of Zn^{2+} on mitochondrial functioning, as indicated by the observed TPEN-mediated reduction of ΔΨ losses, may help to ameliorate the organelle capability to cope with $[Ca^{2+}]_i$ buffering.

To test whether Zn^{2+} chelation is able to promote neuroprotection, viability was assessed in TPEN-treated cultures exposed to NMDA. Viability, evaluated with the lactate dehydrogenase (LDH) efflux assay, showed that TPEN exposure [with a protocol using 1 min pre-incubation at 1 μM, and 10 μM of the compound during the 5 min NMDA (50 μM) + glycine (10 μM) challenge] promoted significant levels of neuroprotection in the 12 h that followed the NMDA treatment (Fig. 5F; 40.1% decreased neuronal loss compared to control). We then tested whether TPEN is neuroprotective by blocking damaging effects of Zn^{2+} on mitochondria. To that aim, we assessed viability in striatal cultures exposed, with or without TPEN, to the same acute excitotoxic paradigm (50 μM NMDA + 10 μM glycine for 5 min) in presence of CCCP [750 nM; here employed to prevent cation uptake (Stout et al., 1998)]. CCCP and TPEN produced no additive effects (Fig. 5F-H), thereby suggesting that mitochondria represent the final and common target for excitotoxic $[Zn^{2+}]_i$ rises to promote damage.

Overall, these results indicate that, in nNOS (-) neurons, TPEN-mediated blockade of Zn^{2+}-dependent injury leads to a neuroprotective outcome that resembles, at least in part, the one found in nNOS (+) neurons where aborted Zn^{2+} mobilization is obtained by the missing production of ROS that follows NMDAR activation.

Discussion

In this study, we have characterized the behavior of nNOS (+) neurons in conditions of prolonged NMDAR activation and employed this cell model to dissect the relative contribution of $[Ca^{2+}]_i$ overload, mitochondrial failure, ROS production, and $[Zn^{2+}]_i$ mobilization in the progression and full development of the excitotoxic cascade. Our results support the central role played by mitochondria in the context of excitotoxicity. However, our findings also integrate steps of the cascade and indicate that ROS-dependent release of $[Zn^{2+}]_i$ is a required intermediate mechanism that acts in close synergy with $[Ca^{2+}]_i$ to promote, especially in the early stages of excitotoxicity, irreversible mitochondrial dysfunctions.

These results provide an additional framework to understand the role of $[Zn^{2+}]_i$ and $[Ca^{2+}]_i$ deregulation in neurological conditions associated with a strong excitotoxic component. This applies to AD progression and development where a damaging interplay between $[Ca^{2+}]_i$, $[Zn^{2+}]_i$, and oxidative stress has been indicated to occur (Corona et al., 2011; McCord and Aizenman, 2014). Zn^{2+}-dependent neuronal injury seems also particularly important in cerebral ischemia as shown in preclinical models of transient global ischemia (Koh et al., 1996) while in vitro experimental evidence has supported a synergistic role for the two cations in acute ischemic conditions, a setting where Ca^{2+} and Zn^{2+} appear to promote, with distinctively different temporal dynamics, neuronal damage and mitochondrial dysfunction (Shuttleworth and Weiss, 2011; Vander Jagt et al., 2009). In that regard, our findings provide further mechanisms of action for the damaging effects of NMDAR-driven deregulation of $[Ca^{2+}]_i$ and related oxidative stress as occurring in cerebral ischemia. In ALS, another neurodegenerative condition associated with oxidative stress and glutamate-driven $[Ca^{2+}]_i$ imbalance (Boillee et al., 2006), the role of Zn^{2+} in MN injury is still largely unexplored; however, the Ca^{2+}-ROS-Zn^{2+} injurious link described here offers a rationale for exploratory studies aiming at unraveling Zn^{2+}-dependent pathways of MN loss. Finally, the neuroprotective mechanisms that we show here to occur in nNOS (+) striatal neurons may help to explain some of the beneficial effects of PBT2, a Zn^{2+} (and copper) chelating compound that has been found, in a recent clinical trial, to promote positive outcomes in HD patients (Huntington Study Group Reach, 2015).

Mitochondrial failure plays a pivotal role in excitotoxic neuronal death

Changes in $[Ca^{2+}]_i$ and mitochondrial functioning were investigated in nNOS (+) neurons exposed to an excitotoxic challenge. Although nNOS (+) neurons possess operational NMDARs (Canzoniero et al., 2013), prolonged NMDAR stimulation in these cells results in $[Ca^{2+}]_i$ loads that are reduced when compared to neighboring nNOS (-) neurons (Fig. 1C and D). Overall, NMDAR-driven $[Ca^{2+}]_i$ rises depend on direct cation flux through the receptor as well as on the concerted activity of intracellular buffering and extrusion mechanisms (Clapham, 1995; Gleichmann and Mattson, 2011). In this context, mitochondria actively promote $[Ca^{2+}]_i$ clearance and represent a major coordinating point for the convergence of apoptotic and necrotic processes (Ankarcrona et al., 1995; Rizzuto et al., 2012; Rizzuto et al., 2003; Schinder et al., 1996), as excessive mitochondrial Ca^{2+} accumulation leads to Ca^{2+}-dependent and mitochondria-mediated neuronal death (Duchen, 2012; Panov et al., 2002).

Our results indicate that the particular milieu possessed by nNOS (+) neurons leads their mitochondria to create a beneficial and divergent point in the excitotoxic cascade. On the contrary of what observed in nNOS (-) neurons, the organelles of nNOS (+) cells are not impaired by NMDAR activation and respond to NMDAR-driven $[Ca^{2+}]_i$ rises with minimal production of ROS and modest $\Delta\Psi$ losses (Fig. 2A-D; Canzoniero et al., 2013). One possible explanation for the phenomenon is that mitochondria of nNOS (+) neurons undergo reduced Ca^{2+} uptake and/or display better cycling of Ca^{2+} between the mitochondrial and cytosolic compartments, a protective mechanism that has been previously reported in neurons exposed to NMDA (Wang and Thayer, 2002). Support for this idea comes from the combined analysis of VGCC-mediated $[Ca^{2+}]_i$ rises, ROS, and $\Delta\Psi$ changes as well as $[Zn^{2+}]_i$ accumulations (Fig. S3). Comparison of immediate (15-30 sec; Fig. 1C and S1) peak levels of $[Ca^{2+}]_i$ rises occurring in striatal cultures exposed to NMDA with the ones triggered by high K^+ (Fig. S3A dashed line) show that nNOS (+) and nNOS (-) neurons respond to receptor or channel activation with Ca^{2+} influxes that are undistinguishable in terms of amounts when cross comparing between the two populations and/or routes of Ca^{2+} entry. What instead differs, when analyzing NMDAR- or VGCC-dependent Ca^{2+} rises in the two populations, is the temporal progression of these $[Ca^{2+}]_i$ elevations. In the case of nNOS (-) neurons, $[Ca^{2+}]_i$

accumulation continues to build up during NMDA exposures, a phenomenon that occurs in minutes and is therefore not linked to receptor-mediated influx but rather indicative of initial perturbations of $[Ca^{2+}]_i$ handling. One possible explanation for the phenomenon is that, within the first few minutes of NMDAR activation, source-specific accumulation of ROS and RNS produces the required oxidative stress that impairs mitochondrial buffering along with the malfunctioning of additional extrusion mechanisms (Bano et al., 2005; Dugan et al., 1995). This assumption is supported by our HEt results where we find that nNOS (-) neurons show a robust ROS production that reaches almost the plateau phase within 5 min of NMDAR stimulation (Fig. 3C). These large ROS rises are occurring along with initial signs of mitochondrial depolarization and $[Zn^{2+}]_i$ release (Fig. 6A). On the contrary, in nNOS (+) neurons the NMDAR-dependent oxidative hit is significantly decreased and associated with concurrent improved $[Ca^{2+}]_i$ handling, minimal $\Delta\Psi$ losses, and abolished $[Zn^{2+}]_i$ rises (Fig. 6B). These combined responses show great analogies with effects of $[Ca^{2+}]_i$ rises triggered by VGCC activation, a maneuver devoid of neurotoxic effects (Fig. 4J). Analysis of downstream effects in depolarized nNOS (+) and nNOS (-) neurons show that VGCC-dependent Ca^{2+} influx, although initially similar to the cation influx observed upon NMDAR activation, fails to promote oxidative stress, thereby aborting $[Zn^{2+}]_i$ mobilization and mitochondrial dysfunction (Fig. S3).

The hypothesis that mitochondria are points of convergence for the injurious NMDAR-dependent Ca^{2+}-ROS- Zn^{2+} deregulation is supported by findings on mitochondrial buffering activity of striatal neurons exposed to NMDA in presence of CCCP (Fig. 2E-G). These experiments show that, in nNOS (+) neurons, inhibition of mitochondrial Ca^{2+} uptake produces post-NMDA $[Ca^{2+}]_i$ changes that are largely similar to the ones observed in nNOS (-) neurons (Fig. 2E-G). These findings strongly suggest that differences in NMDAR-driven $[Ca^{2+}]_i$ accumulations found in nNOS (+) neurons are mostly due to improved mitochondrial Ca^{2+} buffering (Fig. 1C *vs* Fig. 2E). Thus, one can speculate that, because of their capability to largely maintain the $\Delta\Psi$ in response to NMDA-driven $[Ca^{2+}]_i$ rises, nNOS (+) neurons are able to promote improved Ca^{2+} cycling between mitochondrial and cytosolic compartments. This phenomenon is a potentially protective mechanism as prolonged Ca^{2+} accumulation in mitochondria opens the organelle high-conductance mode of the permeability transition pore (Ichas and Mazat, 1998; Miller, 1998), promotes electron transport (McCormack et al., 1990) and increases ROS

production (Castilho et al., 1999; Dugan et al., 1995), all processes leading to an acceleration of the death program. Contrary to nNOS (-) neurons, where mitochondrial Ca^{2+} sequestration triggers prolonged ΔΨ loss, thereby potentially leading to defective Ca^{2+} extrusion through the inactivation of the mitochondrial Na^+/Ca^{2+} exchanger (Palty et al., 2010), nNOS (+) neurons, by largely maintaining their ΔΨ may favor the activation of the exchanger in forward mode. This activation can promote beneficial effects as, according to the model proposed by (Szabadkai and Duchen, 2008), mitochondria are then forced to use the Na^+/H^+ antiporter in order to maintain their Na^+ content (Nicholls and Chalmers, 2004; Szabadkai and Duchen, 2008). In that condition, the Na^+/H^+ may therefore generate a proton influx that results in three positive effects like feeding the electron transport chain, slowing phosphate influx through phosphate carriers, and preventing the formation of hydroxyapatite precipitates within the mitochondrial matrix (de la Fuente et al., 2012).

$[Zn^{2+}]_i$ mobilization links ROS production to mitochondrial failure and $[Ca^{2+}]_i$ deregulation

The Ca^{2+}-ROS-Zn^{2+} injurious link is supported by the comparison of NMDAR-dependent $[Zn^{2+}]_i$ rises that occur in the two striatal subpopulations.

nNOS (+) neurons show greatly reduced $[Zn^{2+}]_i$ mobilization from endogenous pools (Fig. 4A-D). The result is due to the absence of ROS as trigger for the release and not because of the paucity of metallothionein-bound Zn^{2+} as thiol oxidation of these proteins by DTDP produces $[Zn^{2+}]_i$ elevations that are undistinguishable from the ones observed in nNOS (-) neurons (Fig. 4E-H).

The idea that $[Zn^{2+}]_i$ rises, triggered by NMDAR-dependent elevations in $[Ca^{2+}]_i$, ROS, and RNS are needed in the excitotoxic cascade is substantiated by the chelation experiments performed in nNOS (-) neurons. In this set, blockade of excitotoxic $[Zn^{2+}]_i$ rises by TPEN makes nNOS (-) neurons able to mimic the behavior of nNOS (+) cells. In response to an excitotoxic hit, TPEN-treated nNOS (-) neurons show improved $[Ca^{2+}]_i$ buffering, decreased ΔΨ loss, and enhanced viability after the NMDA exposure (Fig. 5A-F). These results are in agreement with previous studies performed on isolated brain mitochondria and mitochondria of acute brain slices undergoing oxygen-glucose deprivation (Jiang et al., 2001; Medvedeva and Weiss, 2014). These evidence

showed that mitochondrial Zn^{2+} uptake critically contributes to the development of mitochondrial failure as well as to delayed and irreversible deregulation of neuronal $[Ca^{2+}]_i$ and death (Clausen et al., 2013; Jiang et al., 2001; Medvedeva et al., 2009; Medvedeva and Weiss, 2014; Vander Jagt et al., 2009). Our study expands these findings and reveals a central role for $[Zn^{2+}]_i$ as the executioner that, once mobilized from intracellular pools, exacerbates $[Ca^{2+}]_i$ deregulation and furthers mitochondrial dysfunction and related oxidative stress (Fig. 5D-E) (Bonanni et al., 2006; Jiang et al., 2001). A recent study has questioned the synergistic activity of Ca^{2+} and Zn^{2+} in promoting excitotoxicity (Pivovarova et al., 2014). The study has suggested that Ca^{2+} plays a major role in promoting glutamate-driven neuronal loss while Zn^{2+} appears to be only marginally involved in the process (Pivovarova et al., 2014). We believe that our data support a major role for Zn^{2+} in excitotoxicity. Discrepancies between the two studies are likely due to differences in the experimental settings. In that respect, in the mentioned study (Pivovarova et al., 2014), the authors explored toxicity triggered by application of exogenous Zn^{2+} along with glutamate in a Ca^{2+}-free medium. The maneuver, was intended to mimic conditions of excessive Zn^{2+} release from presynaptic terminals, but actually recapitulates only in part what is occurring in pathophysiological settings. Application of exogenous Zn^{2+} is questionable as the relevance of synaptic Zn^{2+} has been and still is the object of a heated and unresolved debate as far as molar amounts and pathophysiological relevance of such release (Nydegger et al., 2010; Sensi et al., 2009; Vergnano et al., 2014). More importantly, given the inhibitory activity of Zn^{2+} on NMDARs, this experimental setting is only investigating glutamate-dependent toxicity that results from activation of AMPARs and VGCCs, two stimuli that are devoid of ROS production. Thus, application of Zn^{2+} in a setting where NMDAR activation and Ca^{2+}-dependent oxidative stress are missing fails to reproduce the complexity of the excitotoxic cascade. Instead, intracellular Zn^{2+} chelation, as employed in our paradigm, allows the full investigation of interplay of the two cations in the pathologically-relevant context of NMDAR activation and the simultaneous occurrence of $[Ca^{2+}]_i$ rises and ROS generation. In these conditions, NMDAR stimulation promotes the Ca^{2+}-dependent ROS production along with RNS generation that are instrumental for $[Zn^{2+}]_i$ mobilization. These $[Zn^{2+}]_i$ rises then help to reinforce the deregulatory activity of Ca^{2+} and oxidative stress, thereby ultimately promoting irreversible mitochondrial damage and neuronal loss.

Finally, it should be stressed that, upon NMDAR activation, the reduction of $[Ca^{2+}]_i$ rises and mitochondrial changes observed in TPEN-treated cultures is not perfectly overlapping with the strong effect found in nNOS (+) neurons. The discrepancy is possibly explained by the largely decreased generation of ROS that characterizes nNOS (+) neurons (Canzoniero et al., 2013; Gonzalez-Zulueta et al., 1998). ROS are in fact, by themselves, able to promote mitochondrial failure, mitochondrial membrane permeabilization as well as the initiation of mPTP opening (Galluzzi et al., 2009; He and Lemasters, 2002; Kowaltowski et al., 1996; Kowaltowski et al., 2001; Vercesi et al., 1997; Zorov et al., 2000). Thus, nNOS (+) neurons, in addition of being preserved from injurious Zn^{2+} overload, show supplementary protection from the direct mitochondrial damage promoted by oxidative stress.

Conclusions

The present study indicates that NMDAR-driven activation of Ca^{2+}-, RNS/ROS-, and Zn^{2+}-dependent mitochondrial dysfunction represents a series of coordinated events leading to neuronal injury. Our data corroborate the importance of mitochondria in the excitotoxic process and unravel a central role for $[Zn^{2+}]_i$ in the injurious cascade. The distinct damaging activity of Zn^{2+} offers a valuable and exploitable therapeutic target as pharmacological modulation of $[Zn^{2+}]_i$ can be achieved without interference on $[Ca^{2+}]_i$ homeostasis and signaling while, given the fact that all the Ca^{2+} chelators are (with higher affinity) also Zn^{2+} chelating agents (McCord and Aizenman, 2013; Radford and Lippard, 2013; Rudolf et al., 2003), selective Ca^{2+} chelation cannot be done without producing alterations in physiological Zn^{2+} signaling.

An important additional outcome of the study is that nNOS (+) neurons emerge as a powerful tool that allows the investigation of the excitotoxic cascade in a naively resistant environment, thereby bypassing intrinsic limitations associated with the use of transgenic models and/or siRNA interference procedures. Analysis of the molecular determinants of excitotoxic resistance as occurring in this subpopulation may clarify excitotoxic steps that can serve as novel therapeutic targets for the treatment of excitotoxicity-prone neurological conditions like AD, HD, ALS, and cerebral ischemia.

Acknowledgments

Authors thank Molecular Neurology Unit members for helpful discussions. Authors are grateful to Domenico Ciavardelli and Riccardo Navarra for help with data analysis. SLS is supported by funds from the Italian Department of Education (PRIN 2011). AG is supported by “Marisa Trampuz von Langendorf” Fellowship for Neuroscience.

Figure legends

Fig. 1. nNOS (+) neurons are spared from NMDA-dependent toxicity and show decreased $[Ca^{2+}]_i$ rises upon NMDAR overactivation. (A) Viability assay of striatal neurons exposed to an excitotoxic challenge. Left panels show differential interference contrast (DIC) images of stained nNOS (+) neurons (cells with dark precipitates), middle panels show fluorescence images of PI staining of cultures exposed to 50 µM NMDA + 10 µM glycine for 5 min and evaluated 24 h after, and right panels show merged DIC and PI images. Images are representative of 5 independent experiments (Scale bar = 100 µm). **(B)** Box plots show quantification of images shown in **(A)**. Data were normalized as percentage of viability changes occurring in sham-treated cultures. **(C)** Time course of NMDAR-dependent $[Ca^{2+}]_i$ rises, as assessed with fluo4-FF. Traces represent average responses to a 5 min exposure to 50 µM NMDA + 10 µM glycine of 12 nNOS (+) and 508 nNOS (-) striatal neurons obtained from 6 independent experiments. **(D)** Box plots depict peak $[Ca^{2+}]_i$ values obtained in the two populations. **(E)** Box plots depict cumulative $[Ca^{2+}]_i$ changes expressed as area under the curve (AUC) of arbitrary units (a.u). **(F)** Time course of $[Ca^{2+}]_i$ rises, as assessed with fluo4-FF, following a brief depolarization (60 mM extracellular K^+; 3 sec) in presence of the glutamate receptor inhibitors MK-801 (10 µM) and NBQX (10 µM). Traces represent average responses of 22 nNOS (+) and 719 nNOS (-) striatal neurons obtained from 9 independent experiments. **(G)** Box plots depict $[Ca^{2+}]_i$ peaks obtained in the two populations. **(H)** Box plots depict $[Ca^{2+}]_i$ changes expressed as AUC (a.u.). ** indicate P≤0.01.

Fig. 2. NMDAR-mediated mitochondrial effects in nNOS (+) and nNOS (-) neurons. (A) Left panel shows DIC image of a nNOS (+) neuron (arrowhead). Middle and right panels show pseudocolor images of TMRE fluorescence evaluated in striatal cultures before (t=0'; middle) and after (t=30', right) 5 min exposure to 50 µM NMDA + 10 µM glycine (Scale bar = 100 µm). **(B)** Panels depict magnification of images shown in **(A)**. A nNOS (-) neuron is depicted as representative of average responses found in the general population of striatal neurons (Scale bar = 10 µm). **(C)** Time course of NMDAR-dependent $\Delta\Psi$ loss upon a 5 min exposure to 50 µM NMDA + 10

μM glycine and assessed with TMRE. Traces depict average TMRE responses of 13 nNOS (+) and 628 nNOS (-) striatal neurons obtained from 10 independent experiments. **(D)** Box plots show quantification of data in **(C)**. **(E)** Time course of $[Ca^{2+}]_i$ rises obtained upon 5 min application of 50 μM NMDA + 10 μM glycine and 750 nM CCCP, as assessed with Mag-fura-2. Traces represent average responses of 15 nNOS (+) and 554 nNOS (-) striatal neurons obtained from 6 independent experiments. **(F)** Box plots show $[Ca^{2+}]_i$ peaks obtained in the two populations. **(G)** Box plots show cumulative $[Ca^{2+}]_i$ changes expressed as area under the curve (AUC; a.u.: arbitrary units). **(H)** Time course of post-NMDA $[Ca^{2+}]_i$ changes obtained upon mitochondrial depolarization. After mitochondrial Ca^{2+} uptake induced by NMDA exposure in presence of CPA (10 μM), a endoplasmic reticulum blocker, employed to promote pure mitochondrial Ca^{2+} uptake, mitochondria were depolarized with CCCP (5 μM) and the amount of released Ca^{2+} assessed with the cytosolic dye fluo-4. Inset shows magnification of normalized traces resulting from CCCP stimulation. Traces represent average responses of 15 nNOS (+) and 467 nNOS (-) neurons obtained from 5 independent experiments. **(I)** Box plots depict $[Ca^{2+}]_i$ peaks obtained after CCCP stimulation in the two populations. **(J)** Box plots of $[Ca^{2+}]_i$ dynamics expressed as AUC (a.u.). * indicates $P \leq 0.05$ and ** indicate $P \leq 0.01$.

Fig. 3. NMDAR-mediated ROS production in nNOS (+) and nNOS (-) neurons. **(A)** Upper left panel depicts DIC image of two nNOS (+) neurons (arrowhead). Pseudocolor images show fluorescence of the ROS-sensitive dye HEt imaged before (t=0'; upper right panel) and after (t=30'; lower left panel) a 5 min 50 μM NMDA + 10 μM glycine exposure halted by addition of MK-801 (10 μM; scale bar = 100 μm). **(B)** Lower right panels show magnification of images shown in **(A)**. A nNOS (-) neuron is depicted as representative of the average response of the general population of striatal neurons (Scale bar = 10 μm). **(C)** Time course of NMDAR-mediated ROS production in cultures exposed for 5 min to 50 μM NMDA + 10 μM glycine. Traces depict average responses of 22 nNOS (+) and 691 nNOS (-) neurons obtained from 9 independent experiments. **(D)** Box plots represent HEt peaks obtained in the two populations. **(E)** Box plots depict cumulative HEt fluorescence changes expressed as area under the curve (AUC; a.u.: arbitrary units). ** indicate $P \leq 0.01$.

Fig. 4. NMDAR-mediated $[Zn^{2+}]_i$ rises in nNOS (+) and nNOS (-) neurons. (A) Upper left panel show DIC image of a nNOS (+) neuron (arrowhead). Pseudocolor images show FluoZin-3 fluorescence imaged at baseline (upper right panel) and during (lower left panel) a 5 min exposure to 50 µM NMDA + 10 µM glycine (Scale bar = 100 µm). Inset (lower right panel) depicts magnification of images in **(A)**. A nNOS (-) neuron is shown as representative of the average response of the general population of striatal neurons (Scale bar = 10 µm). **(B)** Time course of $[Zn^{2+}]_i$ rises triggered by 5 min exposure to 50 µM NMDA + 10 µM glycine as assessed with FluoZin-3. Traces represent average responses of 16 nNOS (+) and 952 nNOS (-) striatal neurons obtained from 8 independent experiments. **(C)** Box plots represent peak $[Zn^{2+}]_i$ values obtained in the two populations. **(D)** Box plots depict cumulative $[Zn^{2+}]_i$ changes expressed as area under the curve (AUC; a.u.: arbitrary units). **(E)** Upper left panel show DIC image of three nNOS (+) neurons (arrowhead). Pseudocolor images show FluoZin-3 fluorescence imaged at baseline (upper right panel) and after (lower left panel) a 15 min exposure to DTDP 250 µM (Scale bar = 100 µm). Inset (lower right panel) depicts magnification of images in **(E)**. One nNOS (+) and one nNOS (-) neuron are depicted as representative of the average response of each population (Scale bar = 10 µm). **(F)** Time course of DTDP-dependent $[Zn^{2+}]_i$ rises. Traces represent average responses of 13 nNOS (+) and 470 nNOS (-) neurons obtained from 5 independent experiments. **(G)** Box plots depict $[Zn^{2+}]_i$ peaks in the two neuronal populations. **(H)** Box plots depict cumulative $[Zn^{2+}]_i$ changes expressed as AUC (a.u.). **(I)** Viability of striatal neurons exposed for 20 min to 100 µM $ZnCl_2$, or 60 mM K^+, or 100 µM $ZnCl_2$ + 60 mM K^+. Experiments were performed in presence of MK-801 (10 µM) and NBQX (10 µM), and neuronal viability assessed with PI staining 24 h after the treatment. Upper panels show DIC images of each treatment, middle panels show fluorescence images of PI staining relative to each treatment condition, and lower panels show merged DIC and PI images. Images are representative of 4 independent experiments. nNOS (+) neurons are indicated by arrowheads (Scale bar = 100 µm). **(J)** Bar chart represents quantification of images in **(I)**, data were normalized as percentage of sham-treated control cultures. ** indicate $P \leq 0.01$.

Fig. 5. In nNOS (-) neurons, NMDA-mediated $[Ca^{2+}]_i$ deregulation, ΔΨ loss, and neuronal death are reduced by intracellular Zn^{2+} chelation. (A) Time course of NMDAR-dependent $[Ca^{2+}]_i$ rises, as assessed with fluo-4FF in cultures exposed for 5 min to 50 µM NMDA + 10 µM glycine with (green) or without (blue) TPEN (10 µM), a high affinity Zn^{2+} chelator. Traces represent average response of 451 control and 521 TPEN-treated neurons obtained from 5 control and 6 TPEN experiments. **(B)** Box plots represent $[Ca^{2+}]_i$ peak values. **(C)** Box plots depict cumulative $[Ca^{2+}]_i$ changes expressed as area under the curve (AUC; a.u.: arbitrary units). Note that Zn^{2+} chelation has no effect on the overall fluo-4FF fluorescence despite its known higher affinity for Zn^{+2} compared to Ca^{2+}. **(D)** Time course of NMDAR-dependent ΔΨ loss, as assessed with TMRE. Traces represent average responses of 338 control and 554 TPEN-treated neurons obtained from 4 control and 7 TPEN experiments. **(E)** Box plot depict quantification of data shown in **(D)**. **(F-H)** Viability of striatal neurons exposed to 50 µM NMDA + 10 µM glycine in the presence of 10 µM TPEN (F), 750 nM CCCP (G) or both (H). Neuronal viability was assessed, with LDH efflux assay, 12 h after the challenge. Data are obtained from more than 8 replicates per condition. * indicates P≤0.05 and ** indicate P≤0.01.

Fig. 6. Analysis of the temporal profile of NMDAR-mediated **$[Ca^{2+}]_i$,$[Zn^{2+}]_i$, ROS and** ΔΨ changes **in nNOS (+) and nNOS (-) neurons.** Combined time courses of $[Ca^{2+}]_i$, $[Zn^{2+}]_i$, ΔΨ and ROS alterations occurring in either **(A)** nNOS (-) or **(B)** nNOS (+) neurons exposed to 50 µM NMDA + 10 µM glycine for 5 min. Combined time courses of $[Ca^{2+}]_i$ and ΔΨ changes occurring in the general population of striatal neurons challenged with 50 µM NMDA + 10 µM glycine in the presence **(D)** or in absence **(C)** of TPEN. **(E)** The pictogram illustrates a proposed schematization of the role of Zn^{2+} in the excitotoxic cascade. NMDAR activation promotes massive Ca^{2+} entry and a surge of mitochondrial and extramitochondrial ROS as well as RNS generation; ROS and RNS are instrumental in promoting $[Zn^{2+}]_i$ mobilization from metallothioneins (MTs; a major cytosolic system in charge of Zn^{2+} buffering that is also redox sensitive and prone to Zn^{2+} release upon oxidation). $[Zn^{2+}]_i$ rises act on mitochondria and, in a self-feeding harmful loop, further the organelle impairment to cope with $[Ca^{2+}]_i$ clearance, thereby enhancing $[Ca^{2+}]_i$ deregulation and ROS production. In nNOS (-) neurons, Zn^{2+} chelation mimics the

aborted excitotoxic cascade found in nNOS (+) cells, thereby lending support to the idea that $[Zn^{2+}]_i$ is a regulator of excitotoxicity.

Fig. S1. Early NMDAR-mediated $[Ca^{2+}]_i$ rises in nNOS (-) and nNOS (+)neurons. (A) Graph depict a magnification, with a higher temporal resolution scale, of NMDAR-dependent $[Ca^{2+}]_i$ rises shown in Fig. 1C. Traces represent average responses, assessed with fluo-4FF, of 12 nNOS (+) and 508 nNOS (-) striatal neurons obtained from 6 independent experiments. No statistically significant differences were observed within the first 20 sec of NMDA (50 µM + 10 glycine) exposure in line with what previously reported (Canzoniero et al., 2013). Note that differences in $[Ca^{2+}]_i$ loads between nNOS (-) and nNOS (+) neurons reached statistical significance only for values occurring 90 sec after the challenge. **(B)** Box plots depict $[Ca^{2+}]_i$ peaks obtained in the two populations. **(C)** Box plots depict $[Ca^{2+}]_i$ changes expressed as area under the curve (AUC; a.u.: arbitrary units). n.s. indicates not significant differences (P>0.05).

Fig. S2. VGCC-mediated $[Ca^{2+}]_i$ rises in nNOS (-) and nNOS (+) striatal neurons. (A) Left panel shows DIC image of 4 nNOS (+) neurons (arrowheads). Pseudocolor images show fluo-4FF fluorescence acquired at baseline (middle panel) and during the depolarization phase (right panel; scale bar = 100 µm). Inset depicts magnification of images shown in **(A)**. A nNOS (-) neuron is depicted as representative of the average response of the general population of striatal neurons (Scale bar = 10 µm).

Fig. S3. $[Ca^{2+}]_i$, ROS, $[Zn^{2+}]_i$ and ΔΨ changes obtained upon VGCC activation in nNOS (+) and nNOS (-) neurons. (A) Time course of $[Ca^{2+}]_i$ rises evaluated in fluo-4FF-loaded striatal cultures stimulated with a medium containing 60 mM K^+ (high K^+) in presence of glutamate receptor inhibitors (MK-801 10 µM and NBQX 10 µM). Traces represent average $[Ca^{2+}]_i$ responses of 6 nNOS (+) and 557 nNOS (-) striatal neurons obtained from 4 independent experiments. Dashed line, shown here for comparison, depicts peak $[Ca^{2+}]_i$ rises achieved 30 sec after NMDAR stimulation in the two subpopulation (see Fig. 1C). **(B)** Box plots depict peak $[Ca^{2+}]_i$ values obtained

in the two populations. **(C)** Box plots depict cumulative $[Ca^{2+}]_i$ changes expressed as area under the curve (AUC) of arbitrary units (a.u). **(D)** Time course of ROS production evaluated in HEt-loaded neurons stimulated with a high K^+ medium in presence of 10 µM MK-801 and 10 µM NBQX. Traces represent average responses of neurons [5 nNOS (+) and 389 nNOS (-)] obtained from 3 independent experiments. Dashed line depicts maximal ROS production following a 5 min exposure to 50 µM NMDA + 10 µM glycine in nNOS (-) neurons, as in Fig. 3C. **(E)** Box plots depict HEt peak values obtained in the two populations. **(F)** Box plots depict cumulative HEt fluorescence changes expressed as area under the curve (AUC; a.u.: arbitrary units). **(G)** Time course of $[Zn^{2+}]_i$ rises evaluated in FluoZin-3-loaded neurons stimulated with a high K^+ in presence of 10 µM MK-801 and 10 µM NBQX. Traces represent average $[Zn^{2+}]_i$ responses of 5 nNOS (+) and 239 nNOS (-) striatal neurons obtained from 3 independent experiments. Dashed line depicts the peak $[Zn^{2+}]_i$ rises following a 5 min exposure to 50 µM NMDA + 10 µM glycine in nNOS (-) neurons, as in Fig. 4B. **(H)** Box plots depict peak $[Zn^{2+}]_i$ values obtained in the two populations. **(I)** Box plots depict $[Zn^{2+}]_i$ cumulative changes expressed as area under the curve (AUC; a.u.: arbitrary units). **(J)** Time course of ΔΨ loss evaluated in TMRE-loaded neurons stimulated with a high K^+ medium in presence of 10 µM MK-801 and 10 µM NBQX. Traces represent average responses of striatal neurons [11 nNOS (+) and 255 nNOS (-)] obtained from 3 independent experiments. Dashed line depicts the maximal ΔΨ loss following a 5 min exposure to 50 µM NMDA + 10 µM glycine in nNOS (-) neurons, as in Fig. 2C. **(K)** Box plots depict quantification of TMRE changes relative to (A). Note that high K^+ treatment induces a modest loss of mitochondrial ΔΨ that is roughly ≈50-60% lower than what produced by the NMDA stimulation (see fig. 2C-D for comparison). **(L)** Comparison of TMRE changes triggered by either NMDA (50 µM + 10 glycine) or high K^+ exposures in nNOS (+) neurons. No statistically significant differences were detected between nNOS (+) and nNOS (-) neurons in all experiments ($P>0.05$).

Tab. S1. Results of ANOVA followed by Dunnett's post-hoc test for the cell viability experiment shown in fig. 4J. ns indicates not significant differences; ** indicate $P<0.01$; *** indicate $P<0.001$.

References

Aarts, M., et al., 2002. Treatment of ischemic brain damage by perturbing NMDA receptor- PSD-95 protein interactions. Science. 298**,** 846-50.

Aizenman, E., et al., 2000. Induction of neuronal apoptosis by thiol oxidation: putative role of intracellular zinc release. J Neurochem. 75**,** 1878-88.

Ankarcrona, M., et al., 1995. Glutamate-induced neuronal death: a succession of necrosis or apoptosis depending on mitochondrial function. Neuron. 15**,** 961-73.

Bano, D., et al., 2005. Cleavage of the plasma membrane Na+/Ca2+ exchanger in excitotoxicity. Cell. 120**,** 275-85.

Beal, M. F., et al., 1993. Neurochemical and histologic characterization of striatal excitotoxic lesions produced by the mitochondrial toxin 3-nitropropionic acid. J Neurosci. 13**,** 4181-92.

Bidmon, H. J., et al., 2001. Nitric oxide synthase-I containing cortical interneurons co-express antioxidative enzymes and anti-apoptotic Bcl-2 following focal ischemia: evidence for direct and indirect mechanisms towards their resistance to neuropathology. J Chem Neuroanat. 22**,** 167-84.

Boillee, S., et al., 2006. ALS: a disease of motor neurons and their nonneuronal neighbors. Neuron. 52**,** 39-59.

Bonanni, L., et al., 2006. Zinc-dependent multi-conductance channel activity in mitochondria isolated from ischemic brain. J Neurosci. 26**,** 6851-62.

Bossy-Wetzel, E., et al., 2004. Crosstalk between nitric oxide and zinc pathways to neuronal cell death involving mitochondrial dysfunction and p38-activated K+ channels. Neuron. 41**,** 351-65.

Brennan, A. M., et al., 2009. NADPH oxidase is the primary source of superoxide induced by NMDA receptor activation. Nat Neurosci. 12**,** 857-63.

Canzoniero, L. M., et al., 2013. nNOS(+) striatal neurons, a subpopulation spared in Huntington's Disease, possess functional NMDA receptors but fail to generate mitochondrial ROS in response to an excitotoxic challenge. Front Physiol. 4**,** 112.

Castilho, R. F., et al., 1999. Oxidative stress, mitochondrial function, and acute glutamate excitotoxicity in cultured cerebellar granule cells. J Neurochem. 72**,** 1394-401.

Choi, D. W., 1988. Glutamate neurotoxicity and diseases of the nervous system. Neuron. 1**,** 623-34.

Choi, D. W., 1992. Excitotoxic cell death. J Neurobiol. 23**,** 1261-76.

Choi, D. W., 1996. Ischemia-induced neuronal apoptosis. Curr Opin Neurobiol. 6**,** 667-72.

Clapham, D. E., 1995. Calcium signaling. Cell. 80**,** 259-68.

Clausen, A., et al., 2013. Mechanisms of rapid reactive oxygen species generation in response to cytosolic Ca2+ or Zn2+ loads in cortical neurons. PLoS One. 8**,** e83347.

Corona, C., et al., 2011. New therapeutic targets in Alzheimer's disease: brain deregulation of calcium and zinc. Cell Death Dis. 2**,** e176.

Cowan, C. M., Raymond, L. A., 2006. Selective neuronal degeneration in Huntington's disease. Curr Top Dev Biol. 75**,** 25-71.

Dawson, T. M., et al., 1991. Nitric oxide synthase and neuronal NADPH diaphorase are identical in brain and peripheral tissues. Proc Natl Acad Sci U S A. 88**,** 7797-801.

de la Fuente, S., et al., 2012. Mitochondrial free [Ca(2+)] dynamics measured with a novel low-Ca(2+) affinity aequorin probe. Biochem J. 445**,** 371-6.

Duchen, M. R., 2012. Mitochondria, calcium-dependent neuronal death and neurodegenerative disease. Pflugers Arch. 464**,** 111-21.

Dugan, L. L., et al., 1995. Mitochondrial production of reactive oxygen species in cortical neurons following exposure to N-methyl-D-aspartate. J Neurosci. 15**,** 6377-88.

Ferrante, R. J., et al., 1985. Selective sparing of a class of striatal neurons in Huntington's disease. Science. 230**,** 561-3.

Galluzzi, L., et al., 2009. Mitochondrial membrane permeabilization in neuronal injury. Nat Rev Neurosci. 10**,** 481-94.

Gee, K. R., et al., 2002. Detection and imaging of zinc secretion from pancreatic beta-cells using a new fluorescent zinc indicator. J Am Chem Soc. 124**,** 776-8.

Giacomello, M., et al., 2007. Mitochondrial Ca2+ as a key regulator of cell life and death. Cell Death Differ. 14**,** 1267-74.

Gleichmann, M., Mattson, M. P., 2011. Neuronal calcium homeostasis and dysregulation. Antioxid Redox Signal. 14**,** 1261-73.

Gonzalez-Zulueta, M., et al., 1998. Manganese superoxide dismutase protects nNOS neurons from NMDA and nitric oxide-mediated neurotoxicity. J Neurosci. 18**,** 2040-55.

Group, H. s. D. C. R., 1993. A novel gene containing a trinucleotide repeat that is expanded and unstable on Huntington's disease chromosomes. Cell. 72**,** 971-83.

He, L., Lemasters, J. J., 2002. Regulated and unregulated mitochondrial permeability transition pores: a new paradigm of pore structure and function? FEBS Lett. 512**,** 1-7.

Hope, B. T., et al., 1991. Neuronal NADPH diaphorase is a nitric oxide synthase. Proc Natl Acad Sci U S A. 88**,** 2811-4.

Huntington Study Group Reach, H. D. I., 2015. Safety, tolerability, and efficacy of PBT2 in Huntington's disease: a phase 2, randomised, double-blind, placebo-controlled trial. Lancet Neurol. 14**,** 39-47.

Hyrc, K. L., et al., 2000. Ionic selectivity of low-affinity ratiometric calcium indicators: mag-Fura-2, Fura-2FF and BTC. Cell Calcium. 27**,** 75-86.

Ichas, F., Mazat, J. P., 1998. From calcium signaling to cell death: two conformations for the mitochondrial permeability transition pore. Switching from low- to high-conductance state. Biochim Biophys Acta. 1366**,** 33-50.

Jiang, D., et al., 2001. Zn(2+) induces permeability transition pore opening and release of pro-apoptotic peptides from neuronal mitochondria. J Biol Chem. 276**,** 47524-9.

Koh, J. Y., Choi, D. W., 1987. Quantitative determination of glutamate mediated cortical neuronal injury in cell culture by lactate dehydrogenase efflux assay. J Neurosci Methods. 20**,** 83-90.

Koh, J. Y., Choi, D. W., 1988. Vulnerability of cultured cortical neurons to damage by excitotoxins: differential susceptibility of neurons containing NADPH-diaphorase. J Neurosci. 8**,** 2153-63.

Koh, J. Y., et al., 1986. Neurons containing NADPH-diaphorase are selectively resistant to quinolinate toxicity. Science. 234**,** 73-6.

Koh, J. Y., et al., 1996. The role of zinc in selective neuronal death after transient global cerebral ischemia. Science. 272**,** 1013-6.

Kowaltowski, A. J., et al., 1996. Opening of the mitochondrial permeability transition pore by uncoupling or inorganic phosphate in the presence of Ca2+ is dependent on mitochondrial-generated reactive oxygen species. FEBS Lett. 378**,** 150-2.

Kowaltowski, A. J., et al., 2001. Mitochondrial permeability transition and oxidative stress. FEBS Lett. 495**,** 12-5.

Krzywinski, M., Altman, N., 2014. Visualizing samples with box plots. Nat Methods. 11**,** 119-20.

Landwehrmeyer, G. B., et al., 1995. NMDA receptor subunit mRNA expression by projection neurons and interneurons in rat striatum. J Neurosci. 15**,** 5297-307.

Lau, A., Tymianski, M., 2010. Glutamate receptors, neurotoxicity and neurodegeneration. Pflugers Arch. 460**,** 525-42.

Maret, W., 1994. Oxidative metal release from metallothionein via zinc-thiol/disulfide interchange. Proc Natl Acad Sci U S A. 91**,** 237-41.

Mattson, M. P., et al., 1992. beta-Amyloid peptides destabilize calcium homeostasis and render human cortical neurons vulnerable to excitotoxicity. J Neurosci. 12**,** 376-89.

McCord, M. C., Aizenman, E., 2013. Convergent Ca2+ and Zn2+ signaling regulates apoptotic Kv2.1 K+ currents. Proc Natl Acad Sci U S A. 110**,** 13988-93.

McCord, M. C., Aizenman, E., 2014. The role of intracellular zinc release in aging, oxidative stress, and Alzheimer's disease. Front Aging Neurosci. 6**,** 77.

McCormack, J. G., et al., 1990. Role of calcium ions in regulation of mammalian intramitochondrial metabolism. Physiol Rev. 70**,** 391-425.

Medvedeva, Y. V., et al., 2009. Intracellular Zn2+ accumulation contributes to synaptic failure, mitochondrial depolarization, and cell death in an acute slice oxygen-glucose deprivation model of ischemia. J Neurosci. 29**,** 1105-14.

Medvedeva, Y. V., Weiss, J. H., 2014. Intramitochondrial Zn2+ accumulation via the Ca2+ uniporter contributes to acute ischemic neurodegeneration. Neurobiol Dis. 68**,** 137-44.

Miller, R. J., 1998. Mitochondria - the Kraken wakes! Trends Neurosci. 21**,** 95-7.

Nicholls, D. G., 2009. Mitochondrial calcium function and dysfunction in the central nervous system. Biochim Biophys Acta. 1787**,** 1416-24.

Nicholls, D. G., Chalmers, S., 2004. The integration of mitochondrial calcium transport and storage. J Bioenerg Biomembr. 36**,** 277-81.

Nydegger, I., et al., 2010. Zinc is externalized rather than released during synaptic transmission. ACS Chem Neurosci. 1**,** 728-736.

Olney, J. W., 1969. Brain lesions, obesity, and other disturbances in mice treated with monosodium glutamate. Science. 164**,** 719-21.

Palty, R., et al., 2010. NCLX is an essential component of mitochondrial Na+/Ca2+ exchange. Proc Natl Acad Sci U S A. 107**,** 436-41.

Panov, A. V., et al., 2002. Early mitochondrial calcium defects in Huntington's disease are a direct effect of polyglutamines. Nat Neurosci. 5**,** 731-6.

Paoletti, P., et al., 2013. NMDA receptor subunit diversity: impact on receptor properties, synaptic plasticity and disease. Nat Rev Neurosci. 14**,** 383-400.

Parsons, M. P., Raymond, L. A., 2014. Extrasynaptic NMDA receptor involvement in central nervous system disorders. Neuron. 82**,** 279-93.

Pivovarova, N. B., et al., 2014. The interactive roles of zinc and calcium in mitochondrial dysfunction and neurodegeneration. J Neurochem. 128**,** 592-602.

Price, R. H., Jr., et al., 1993. Nitric oxide synthase neurons in rat brain express more NMDA receptor mRNA than non-NOS neurons. Neuroreport. 4**,** 807-10.

Radford, R. J., Lippard, S. J., 2013. Chelators for investigating zinc metalloneurochemistry. Curr Opin Chem Biol. 17**,** 129-36.

Rizzuto, R., et al., 2012. Mitochondria as sensors and regulators of calcium signalling. Nat Rev Mol Cell Biol. 13**,** 566-78.

Rizzuto, R., et al., 2003. Calcium and apoptosis: facts and hypotheses. Oncogene. 22**,** 8619-27.

Ross, C. A., Tabrizi, S. J., 2011. Huntington's disease: from molecular pathogenesis to clinical treatment. Lancet Neurol. 10**,** 83-98.

Rothman, S. M., Olney, J. W., 1986. Glutamate and the pathophysiology of hypoxic--ischemic brain damage. Ann Neurol. 19**,** 105-11.

Rothstein, J. D., et al., 1995. Selective loss of glial glutamate transporter GLT-1 in amyotrophic lateral sclerosis. Ann Neurol. 38**,** 73-84.

Rudolf, R., et al., 2003. Looking forward to seeing calcium. Nat Rev Mol Cell Biol. 4**,** 579-86.

Sattler, R., et al., 1997. Determination of the time course and extent of neurotoxicity at defined temperatures in cultured neurons using a modified multiwell plate fluorescence scanner. J Cereb Blood Flow Metab. 17**,** 455-63.

Sattler, R., et al., 1999. Specific coupling of NMDA receptor activation to nitric oxide neurotoxicity by PSD-95 protein. Science. 284**,** 1845-8.

Schindelin, J., et al., 2012. Fiji: an open-source platform for biological-image analysis. Nat Methods. 9**,** 676-82.

Schinder, A. F., et al., 1996. Mitochondrial dysfunction is a primary event in glutamate neurotoxicity. J Neurosci. 16**,** 6125-33.

Sensi, S. L., et al., 1997. Measurement of intracellular free zinc in living cortical neurons: routes of entry. J Neurosci. 17**,** 9554-64.

Sensi, S. L., et al., 2009. Zinc in the physiology and pathology of the CNS. Nat Rev Neurosci. 10**,** 780-91.

Sensi, S. L., et al., 2003. Modulation of mitochondrial function by endogenous Zn2+ pools. Proc Natl Acad Sci U S A. 100, 6157-62.

Sensi, S. L., et al., 2000. AMPA/kainate receptor-triggered Zn2+ entry into cortical neurons induces mitochondrial Zn2+ uptake and persistent mitochondrial dysfunction. Eur J Neurosci. 12, 3813-8.

Shuttleworth, C. W., Weiss, J. H., 2011. Zinc: new clues to diverse roles in brain ischemia. Trends Pharmacol Sci. 32, 480-6.

Stout, A. K., et al., 1998. Glutamate-induced neuron death requires mitochondrial calcium uptake. Nat Neurosci. 1, 366-73.

Szabadkai, G., Duchen, M. R., 2008. Mitochondria: the hub of cellular Ca2+ signaling. Physiology (Bethesda). 23, 84-94.

Uemura, Y., et al., 1990. Selective sparing of NADPH-diaphorase-somatostatin-neuropeptide Y neurons in ischemic gerbil striatum. Ann Neurol. 27, 620-5.

Vander Jagt, T. A., et al., 2009. Intracellular Zn2+ increases contribute to the progression of excitotoxic Ca2+ increases in apical dendrites of CA1 pyramidal neurons. Neuroscience. 159, 104-14.

Vercesi, A. E., et al., 1997. The role of reactive oxygen species in mitochondrial permeability transition. Biosci Rep. 17, 43-52.

Vergnano, A. M., et al., 2014. Zinc dynamics and action at excitatory synapses. Neuron. 82, 1101-14.

Wang, G. J., Thayer, S. A., 2002. NMDA-induced calcium loads recycle across the mitochondrial inner membrane of hippocampal neurons in culture. J Neurophysiol. 87, 740-9.

Yu, S. P., et al., 2001. Ion homeostasis and apoptosis. Curr Opin Cell Biol. 13, 405-11.

Zhao, J., et al., 2008. The zinc indicator FluoZin-3 is not perturbed significantly by physiological levels of calcium or magnesium. Cell Calcium. 44, 422-6.

Zorov, D. B., et al., 2000. Reactive oxygen species (ROS)-induced ROS release: a new phenomenon accompanying induction of the mitochondrial permeability transition in cardiac myocytes. J Exp Med. 192, 1001-14.

Figure 1

Click here to download high resolution image

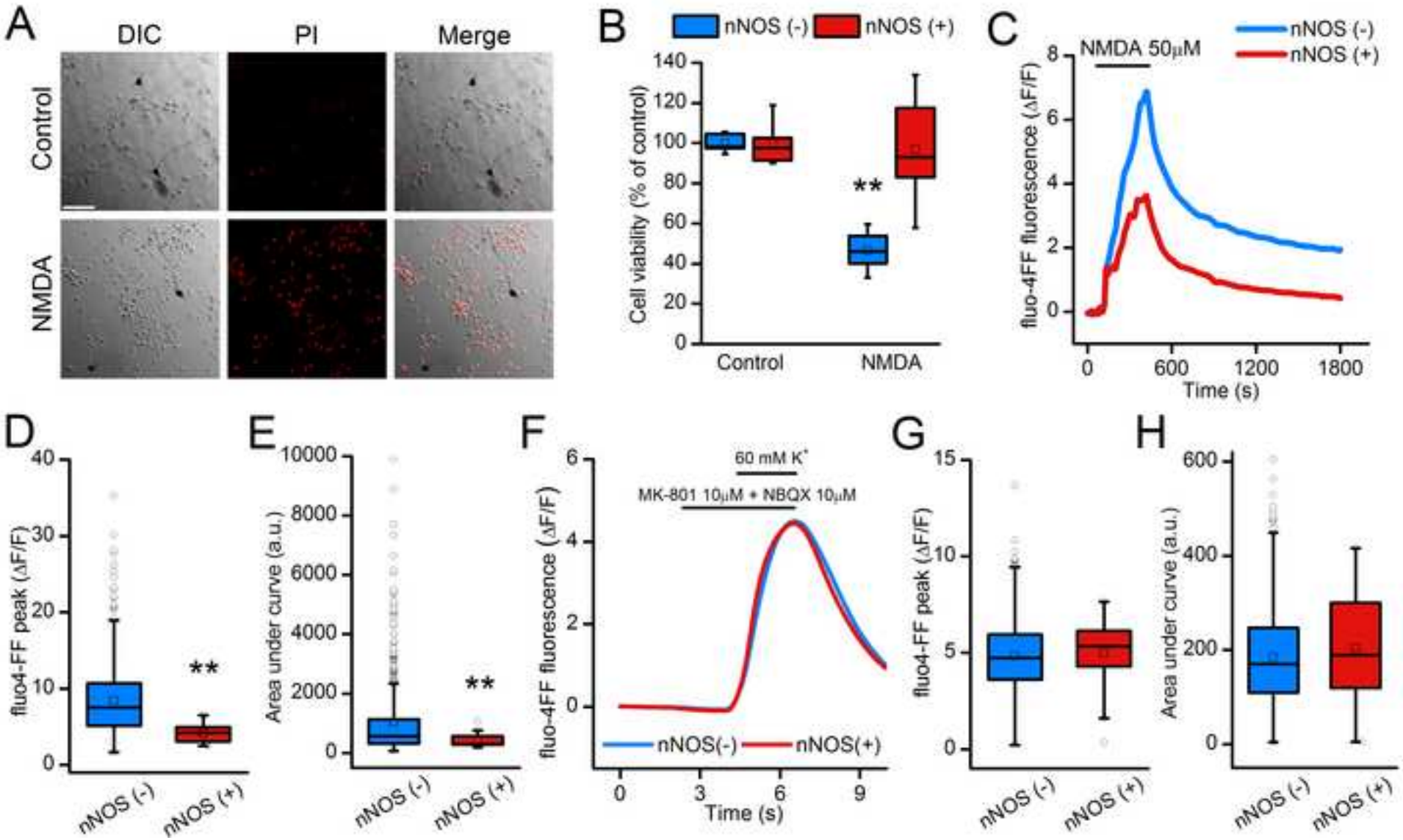

Figure 2

Click here to download high resolution image

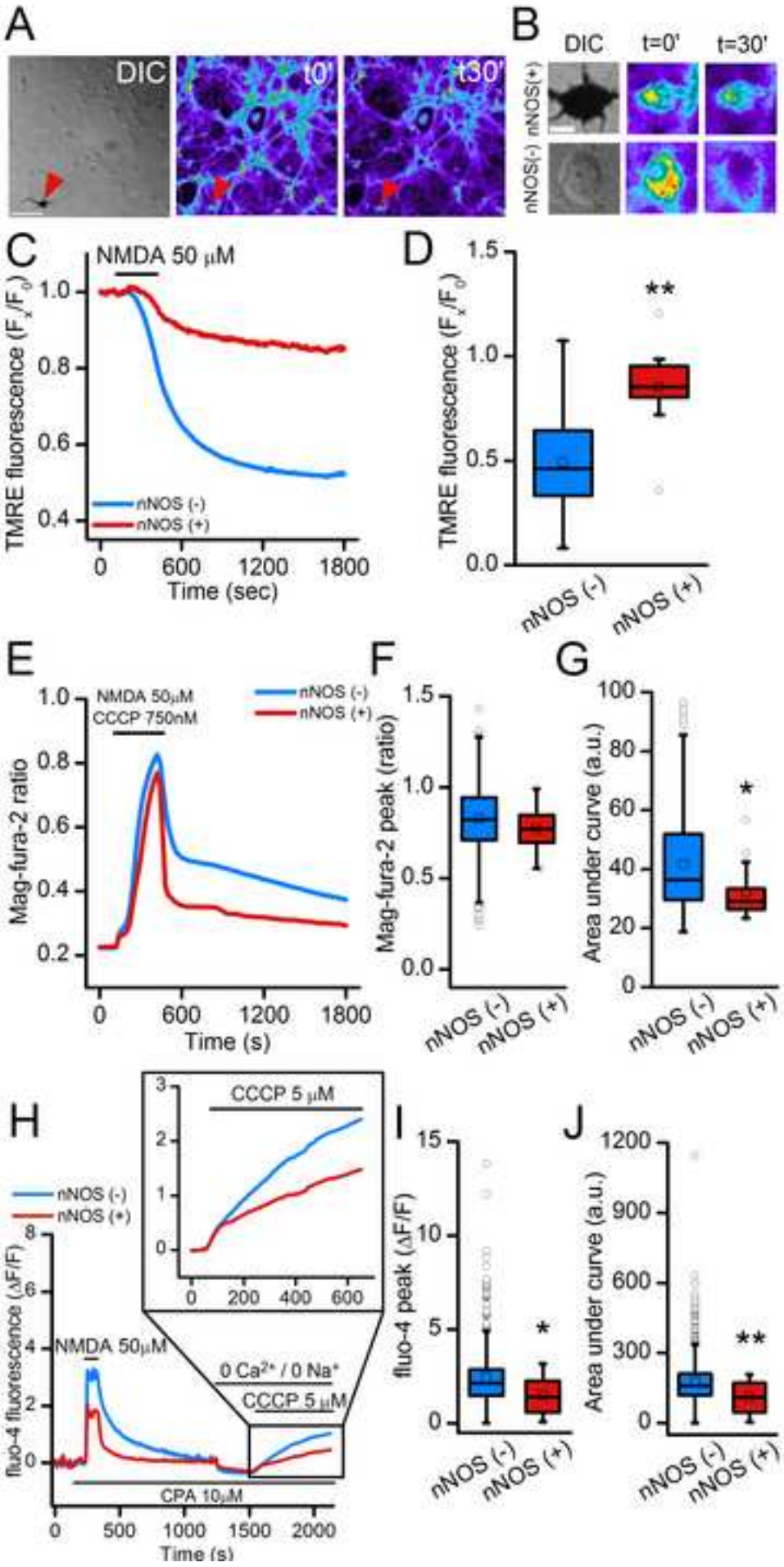

Figure 3

Click here to download high resolution image

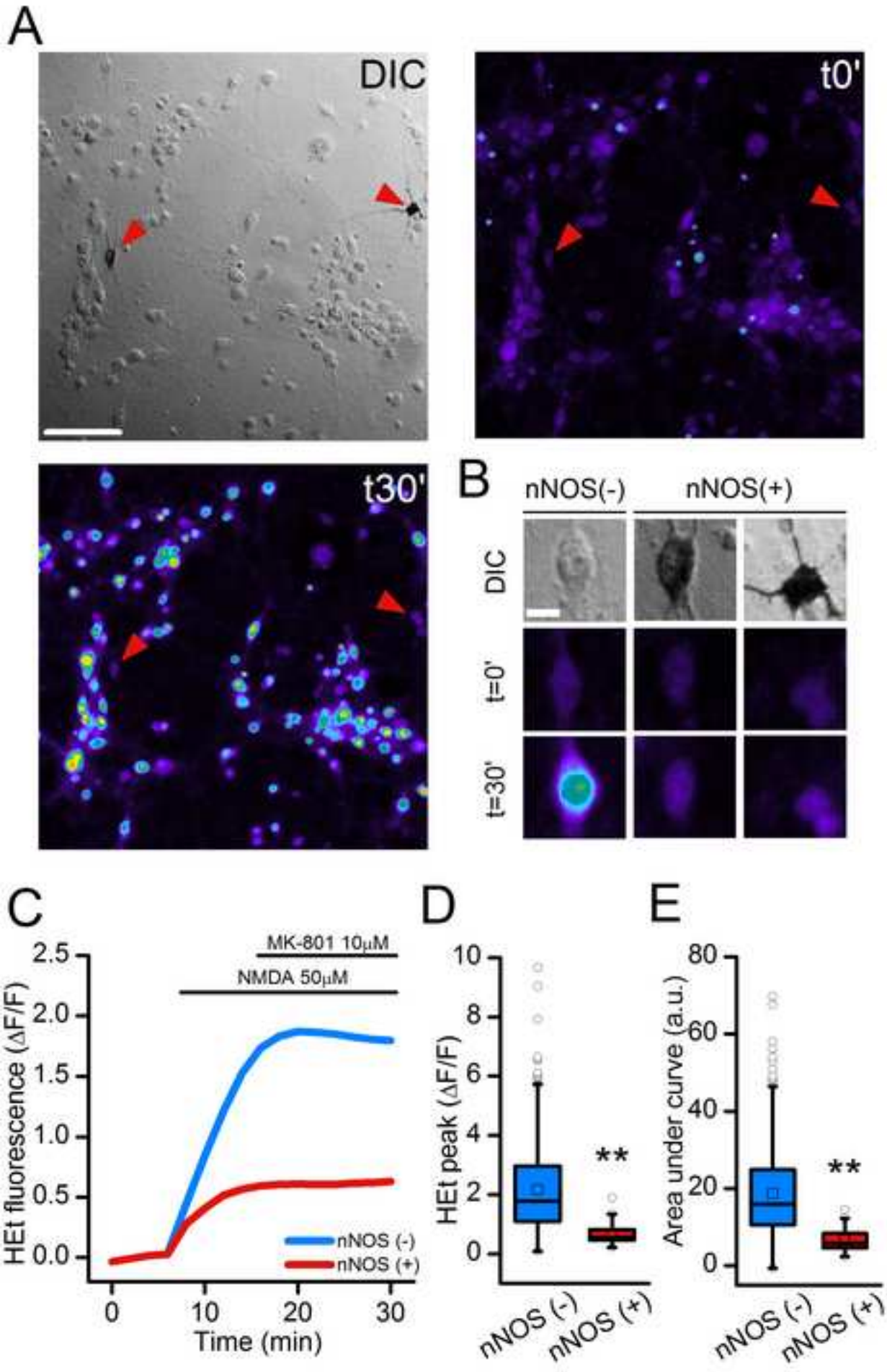

Figure 4

Click here to download high resolution image

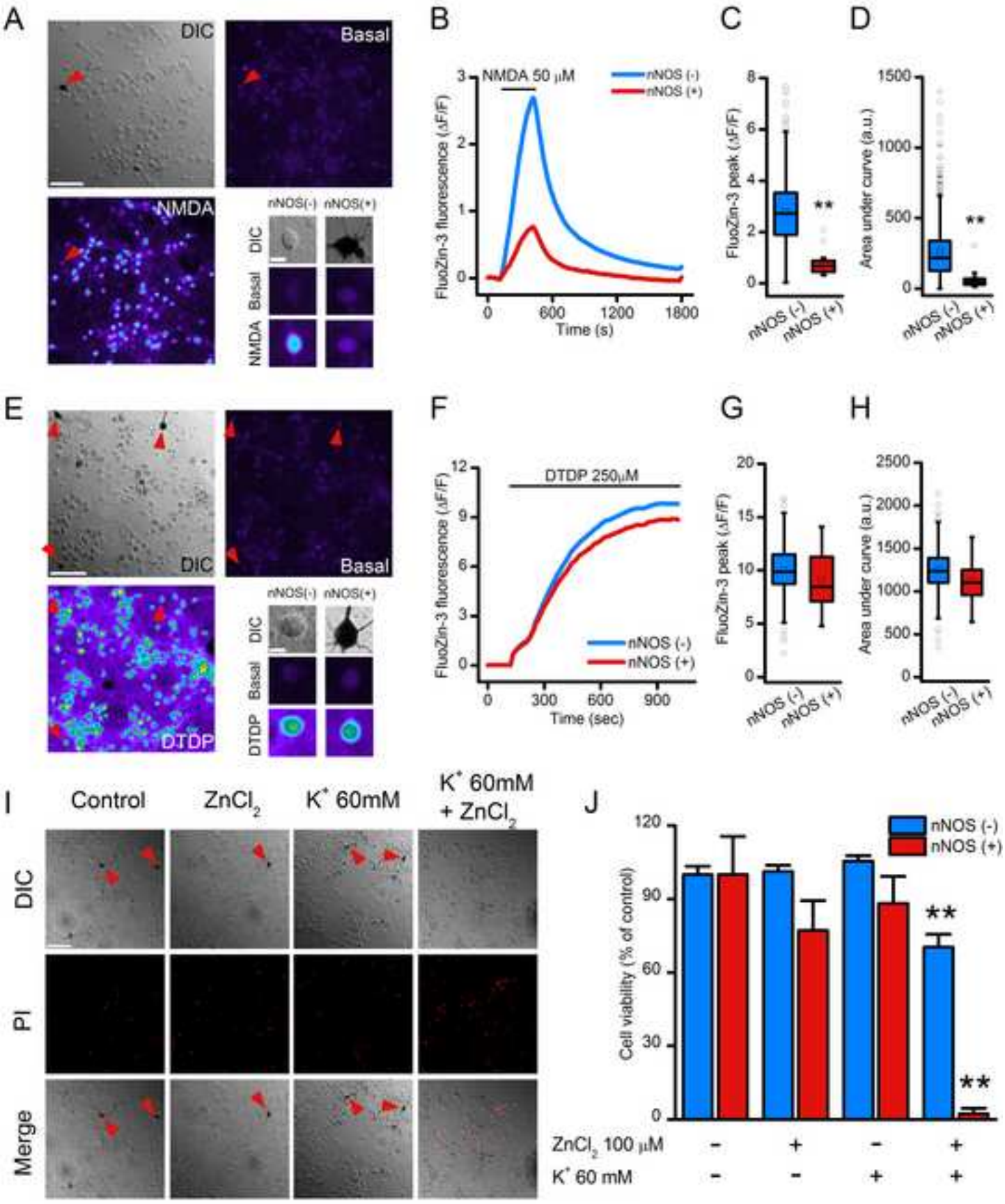

Figure 5

Click here to download high resolution image

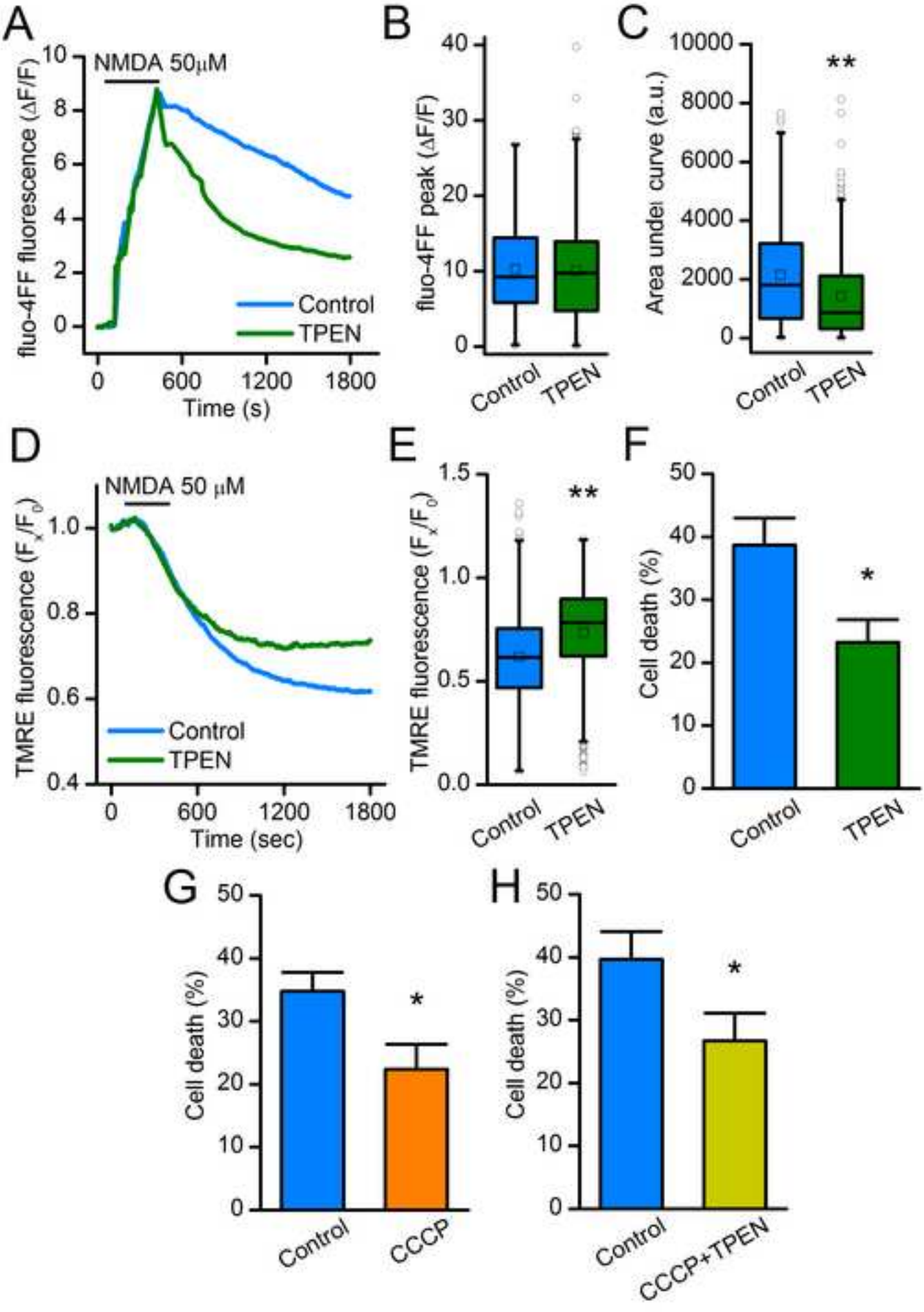

Figure 6

Click here to download high resolution image

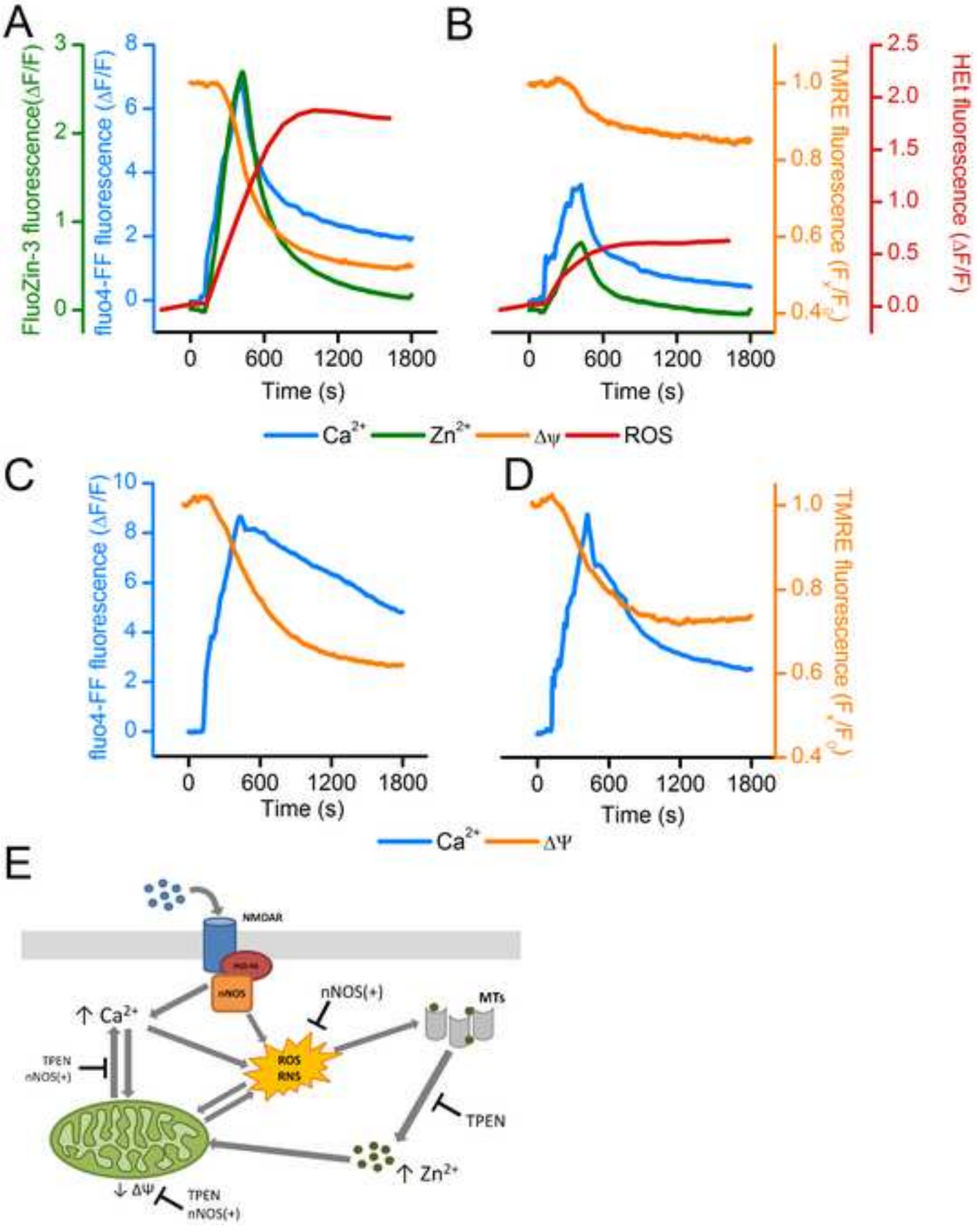

Supplementary Material S1

Click here to download Supplementary Material: S1.tif

Supplementary Material S2

Click here to download Supplementary Material: S2.tif

Supplementary Material S3

Click here to download Supplementary Material: S3.tif

Supplementary Material Tab. 1

Click here to download Supplementary Material: Suppl. Tab. 1.docx